International Journal of Disaster Risk Reduction 100 (2024) 104163

Contents lists available at ScienceDirect

International Journal of Disaster Risk Reduction

journal homepage: www.elsevier.com/locate/ijdrr

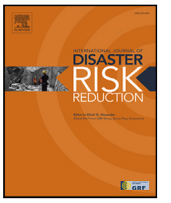

A numerical methodology for estimating site-specific cascading earthquake and tsunami dynamic loading on critical infrastructure

Cláudia Reis [a,*], André R. Barbosa [a], Maria Ana Baptista [b], Mário Lopes [c], Stéphane Clain [d]

[a] School of Civil and Construction Engineering, Oregon State University, Corvallis, OR 97330, United States of America
[b] Instituto Superior de Engenharia de Lisboa, Instituto Politécnico de Lisboa, R. Conselheiro Navarro 1, 1959-007 Lisboa, Portugal
[c] Civil Engineering Research and Innovation for Sustainability, CERIS, Instituto Superior Técnico, Universidade de Lisboa, Avenida Rovisco Pais, 1, 1049-001 Lisboa, Portugal
[d] Departamento de Matemática, Universidade de Coimbra, 3000-393 Coimbra, Portugal

ARTICLE INFO

Dataset link: https://www.gebco.net/, https://www.kyoshin.bosai.go.jp/, https://www.ngdc.noaa.gov/

Keywords:
Port
Cascading hazard
Earthquake
Tsunami

ABSTRACT

A numerical methodology for deriving cascading earthquake and tsunami loading patterns for use in critical infrastructure design is proposed. Earthquake source parameters are first used to generate synthetic ground motion acceleration time series at the site of a critical infrastructure using an open-source stochastic extended finite-source simulation algorithm. Using the same earthquake source information, the tsunami phases of generation, propagation, and inundation are modeled using a coupling approach for determining tsunami wave forces. The coupling approach combines (1) a code based on non-linear shallow water equations solved by the Finite Volume method, which is used to capture the tsunami flow characteristics from generation through the inundation phase until relatively close to the structure, coupled with (2) an open-source computational fluid simulation code, which relies on solving the Navier–Stokes equations using the Smoothed Particle Hydrodynamics method. An appendix presents the validation of the numerical methodology through correlation of the numerical simulations with field data recorded during the 2011 Japan Earthquake and Tsunami. The methodology is then employed to characterize the ground shaking and tsunami loading patterns at the site of the container terminal of the Sines deep-water seaport in Portugal, when subjected to the historic 1755 Great Lisbon Earthquake and Tsunami plausible scenarios. For the site, the generated ground motion acceleration time series show peak accelerations exceeding Eurocode 8 design values. Tsunami flow depths and velocities were computed in horizontal and vertical directions and could be used in the assessment of the existing infrastructure or the design of the future expansion of the port.

1. Introduction

Critical infrastructure encompasses a range of services vital to the well-being of the community, including power, fuel, water, communication, public health, major transportation infrastructure, and essential government operations. They encompass both public and private infrastructure that a community deems crucial for providing vital services, safeguarding vulnerable populations, and delivering other important services that benefit the community [1–4]. In the US, for example, critical infrastructure refers to

* Corresponding author.
E-mail address: claudia.reis@oregonstate.edu (C. Reis).

https://doi.org/10.1016/j.ijdrr.2023.104163
Received 23 July 2023; Received in revised form 27 November 2023; Accepted 28 November 2023
Available online 1 December 2023

buildings and structures identified by federal, state, local, or tribal authorities as indispensable for the effective execution of response and recovery management plans, as well as for the ongoing operation of a community.

In a first step towards characterizing community resilience, the assessment of critical infrastructure relies on targeted, accurate multi-hazard characterization [5]. Consequences of misconducted and/or desegregated hazard assessments were highlighted by past events, as reported in surveys taken after Chile 2010 and Japan 2011 events [6,7]. Despite the difficulties in identifying and separating the effects of cascading earthquakes and tsunamis on coastal infrastructure [8,9], the conclusions of the surveys were that, when examining structural performance, interdependencies between hazards should be considered instead of individual hazards.

Cheng et al. [10] investigated the resilience of complex engineered systems and critical infrastructure subjected to multi-hazards as a function of design performance criteria. However, the dynamic variability of physical, seasonal, economical, industrial and sociopolitical factors influencing hazard assessment of the region is identified as a challenge due to the large number of scenarios deemed necessary to cover all the combinations to assure the performance of the system(s). Argyroudis et al. [11] performed a resilience assessment of infrastructure to extreme events and sequences of diverse hazards for maintaining the functionality of transport assets. The study generated fragility and restoration functions for individual and combined hazards However, and for the sake of predictability, the validation of these functions is limited by the paucity of recorded data and integrated inputs from experts, owners, stakeholders and engineers. In the particular context of maritime transportation, ports play a critical role [12]. Verchuur et al. [13,14] characterized multi-hazard risk of port infrastructures and trade risk in terms of logistics losses as a consequence of interrupting maritime trade. However, different types of ports and geographical locations are associated with different responses to natural hazards. The importance of having a more complete database of global ports recovery in case of emergency is referred as an essential part to provide a more holistic view of the supply-chain impacts and recovery due to port disruptions. For example, Suppasri et al. [15] listed the behavior of ports surveyed after major damaging tsunamis that occurred in Japan and Indonesia, allowing to introduce relationships between natural hazard impact and failure of critical infrastructure. However, and due to the infrequent nature of such extreme events, synthetic data contributes to understand vulnerability scenarios. Reis et al. 2022a [5] developed a numerical methodology to characterized the cascading earthquake and tsunami (ET) multi-hazard targeting coastal infrastructure. Among other infrastructure, the methodology was adopted to predict the structural behavior of the current and future infrastructure composing a cargo hub of a deep-water seaport. According to these studies, critical infrastructure systems must be designed under extreme and dynamic multi-hazard conditions to prevent disruptions and thereby designed for enhanced resilience. Moreover, some of these critical infrastructure systems also play a lifeline role in case of emergency response of communities, i.e. the vulnerability of such systems to cascading earthquake and tsunami may also significantly jeopardize short- and long-term community resilience (safety and recovery).

Port design and emergency planning rarely considers tsunami and cascading earthquake and tsunami hazards, while coastal protection structures are usually built to mitigate less energetic storm waves [16,17]. The infrequency of earthquake and tsunami extreme events and the complexity of multi-physics phenomena are sources of uncertainty when designing coastal infrastructure. Even though remarkable advances in physical and numerical simulations have contributed to our understanding of these phenomena, additional work is still needed to include the large amounts of physical processes and interactions among multi-scale domains, such as in the propagation of seismic and tsunami waves and the interaction with the natural and built environment on coastal sites. Site conditions, such as soil characteristics and topo-bathymetry, can influence cascading seismic and tsunami loading exerted on infrastructure and, consequently, their structural response. Moreover, multi-hazard assessments commonly characterize seismic ground accelerations and tsunami inundation depth, neglecting the time-dependency and tsunami hydrodynamic quantities [18]. Thus, considering multi-hazard characterization and the determination of the respective design loading pattern constitute a major contribution to informed decision-making for earthquake and tsunami risk and emergency management.

Reis et al. [5] performed deterministic worst-case scenario multi-hazard assessments for various leading earthquake and tsunami intensity measures, such as peak ground accelerations (PGA), free-surface elevation (η) and momentum flux (M_F). The study included regional and local tsunamigenic earthquake faults, generating ground motion strong shaking, tsunami inundation during inflow and outflow stages of a tsunami, and the impact of these hazards on multiple configurations resembling the current and future configurations of a port cargo hub. Important insights were provided for raising awareness for the port risk management by linking geo-hazards to engineering aspects. Additionally, insights on the inter-dependencies of seismic and tsunami effects on the coastal infrastructure were also highlighted. In Reis et al. peak forces due to seismic loading were estimated using ground motion prediction equations (GMPEs) and tsunami hydrostatic and hydrodynamic flow depth and velocity quantities were obtained using finite volume simulations, which were used to determine peak tsunami forces acting on the structural components. However, the dynamic nature of the cascading loading was not characterized and details on the fluid–soil-structural behavior were left unexplored.

Based on the existing knowledge, the objective of this paper is to provide a methodology for determining scenario based, consistent time series of earthquake ground shaking and tsunami forces for the use in assessment and design of critical infrastructure. The methodology consists of several steps. In the first step, the generation of synthetic time series of seismic accelerations is carried out using the open-source EXSIM software, which adopts the stochastic extended finite-fault method [19] and relies on existing ground motion models (GMM). In the second step, time series of tsunami forces are developed using a validated coupled approach [20,21], where simulations of tsunami generation and propagation are performed using an Eulerian-based numerical scheme based on the Finite Volume (FV) method to solve the system of Non-linear Shallow Water equations (NLSW) [22,23], while the simulation of fluid–structure interactions are performed using a Lagrangian-based numerical scheme based on the Smooth Particle Hydrodynamic method (SPH) that solves the Navier–Stokes (NS) system of equations [24,25]. An example case study is provided in the context of international maritime traffic, specifically focusing on the container terminal of the Port of Sines in Portugal.

2. Methodology

In this paper, the conceptual methodology proposed in Reis et al. [26] is extended to derive consistently generated time series of earthquake ground shaking accelerations and tsunami forces. In this methodology, first, a stochastic extended finite-fault algorithm for ground-motion simulation is used to generate time-history of ground shaking accounting for source, path, and site conditions [19]. Second, tsunami forces are numerically generated using an Eulerian–Lagrangian coupled approach [20]. The coupling made between larger and smaller sub-domains is achieved by prescribing Dirichlet boundary conditions intrinsic to each model using hydrodynamic quantities captured by virtual gauges (VG) implemented at strategic locations of the domain [20]. The larger spatial and temporal scale subdomain of tsunami generation and propagation is computed using a NLSW-FV method [22,23], while the highly non-linear phenomena associated with smaller spatial and temporal scale subdomain use to capture the tsunami wave interaction with coastal structures is computed using the NS-SPH method [21,24,25]. Additional details on the methods are provided in Sections 2.1 and 2.2 for completeness.

Appendix includes the correlation between numerical solutions of seismic and tsunami quantities with data recorded from the 2011 Japan Earthquake and Tsunami. An example of the validation of the NS-SPH method for tsunami wave to structure interaction problems can be found in [21].

The application example detailed in Section 3 focuses on the container terminal of the Sines port (pile-supported quay), Portugal, which is a critical infrastructure located in a local and regional tsunami-prone region.

2.1. Ground motion finite-fault model

The EXSIM tool used to conduct the simulations is a stochastic extended finite-fault algorithm for ground-motion simulation. EXSIM is used in this study to generate the ground motion time series [19,27]. The fundamental concept of the EXSIM algorithm is the fault modeling into sub-faults, where each sub-fault is considered a small point source, calculated by the stochastic point-source method [28]. The contributions of each of the N sub-faults are then normalized and a time adjustment is applied to control high- and low-frequency amplitudes. The sum of the various contributions gives the total seismic ground motion accelerations at the site following Eq. (1):

$$A(t) = \sum_{i=l}^{nl} \sum_{j=l}^{nw} H_{ij} \times A_{ij}(t - \Delta t_{ij}) \tag{1}$$

where, nl and nw are the number of sub-faults along the length and width of the main fault, respectively, H_{ij} is a normalization factor for the ijth sub-fault that aims to conserve energy, and Δt_{ij} is the relative time delay for the radiated wave from the ijth sub-fault to reach the observation point.

The model of the total radiation is based on the spectrum of the ground motion at a specific site with the contributions of the complementary physical processes of seismic source generation, path propagation, and site effects, as defined by Boore [28,29] (Eq. (2)), and is given by:

$$A(M_0, R, f) = S(M_0, f) \cdot P(R, f) \cdot G(f) \cdot I(f) \tag{2}$$

where $S(M_0, f)$ is the displacement source spectrum representing the source geometry and spectral characteristics in the source vicinity, $P(R, f)$ captures path influences, the $G(f)$ accounts for site effects, and $I(f)$ is the "instrument" or type of motion considered, where f is frequency of the seismic wave.

The source spectrum is commonly modeled using the Ω−square approach [30], which relates the seismic moment (M_0), and the corner frequency (f_0), assuming $M_0 f^3$ is constant. The constant is related to the stress drop parameter, $\Delta\sigma$, to establish Eq. (3):

$$f_0 = 4.9 \times 10^6 \beta \sqrt[3]{\frac{\Delta\sigma}{M_0}} \tag{3}$$

The 2015 version of EXSIM algorithm normalizes the sub-fault contributions and applies the time adjustments to control high- and low-frequency amplitudes and sums them to obtain the total seismic signal at the site. For each sub-fault, the seismic moment, $M_{0,ij}$, corner-frequency, $f_{c,ij}$, and normalization factor H_{ij} are derived from the total moment, M_0, and slip distributions among the ijth sub-faults, s_{ij}. The $M_{0,ij}$ reads as Eq. (4):

$$M_{0,ij} = \frac{M_0 \times s_{ij}}{\sum_{i=l}^{nl} \sum_{j=l}^{nw} s_{ij}} \tag{4}$$

Mathematically, $f_{c,ij}$ is given by Eq. (5):

$$f_{c,ij} = 4.9 \times 10^6 \beta \left[\frac{N \cdot \Delta\sigma}{N_R \cdot M_0} \right]^{(1/3)} \tag{5}$$

where N_R is the number of fractured sub-faults when the rupture front reaches the ith sub-fault source.

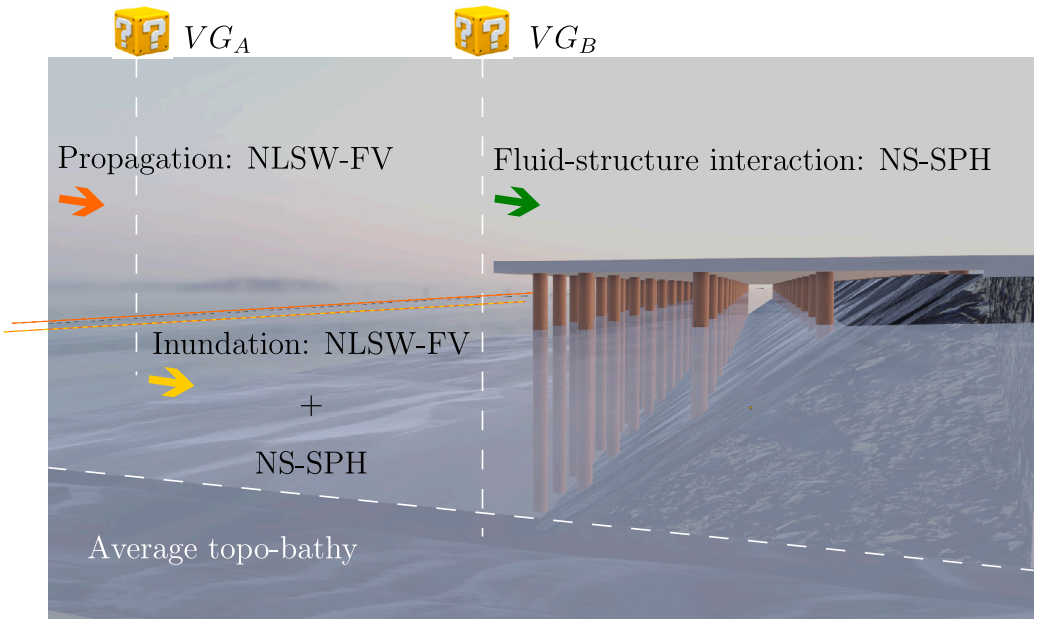

Fig. 1. Methodology: Multi-scale and -physics domains from ET genesis to interaction with the coastal infrastructure. Virtual gauges (VG) are responsible for capturing physical quantities and prescribing open boundary conditions (OBC) among the sub-domains. Imagery rendering using Blender engine [31].

The normalization factor, H_{ij}, represents the delay associated with the travel time between sub-faults to conserve high-frequency amplitudes, is given by Eq. (6):

$$H_{ij} = \frac{M_0}{M_{0,ij}} \sqrt{\frac{\sum_k \left(\frac{f_0^2 f_k^2}{f_0^2 + f_k^2} \right)^2}{N \sum_k \left(\frac{f_{0,ij}^2 f_k^2}{f_{0,ij}^2 + f_k^2} \right)^2}} \tag{6}$$

where f_0 and M_0 are respectively the corner frequency and seismic moment of the whole fault, while $f_{0,ij}$ and $M_{0,ij}$ are the relative to each sub-source. The f_k is the kth frequency ordinate.

The efficacy and efficiency of the EXSIM tool was assessed by correlating numerical solutions and data recorded during the 2011 Japan Earthquake. The validation process is presented in Appendix A.1.

In the application study described below, the EXSIM simulations provide solutions of ground motion acceleration at the bedrock level of the container terminal foundations of a pile-supported quay. Even though EXSIM was used, the methodology is generic enough and can integrate other approaches capable of generating synthetic accelerograms to model other sites and earthquake events.

2.2. Hydrodynamic coupled model

The hydrodynamic simulations were set to provide solutions of tsunami horizontal and vertical forces exerted on vertical and horizontal components in critical infrastructure.

Fig. 1 depicts the coupled multi-scale and multi-physics domains used in this methodology. The full description of the implemented method, including the validation of the coupling scheme using data instrumentally acquired during an experimental campaign at Oregon State University can be found in Reis et al. 2021 [20]. One of the findings in Reis et al. was that computational costs were reduced by 50% due to the one third reduction of the SPH domain when solving fluid–structure interaction problems. The potential optimization of computational resources relying on the coupled scheme significantly increases in real models of oceanic tsunami propagation and inundation, in which simplified models are used to solve problems with spatial scales of hundreds of km and temporal scales of hours. More sophisticated numerical schemes detailing structural-scale domains were then adopted to enhance inundation models to include the interaction between the fluid and the natural and built environment. The main features of the hydrodynamic modeling methodology are detailed next.

The simulations of tsunami generation and propagation compute the tsunami free-surface elevation, η, and flow velocity, u, at the various virtual gauges VG. The tsunami initial condition assumes that the free-surface elevation at instant $t = 0\,\mathrm{s}$ mimics the ocean floor displacements [32]. The computation of the co-seismic displacement follows the Okada's half-space theory [33], implemented in Mirone software [34]. The simulations of tsunami propagation are carried out using a validated numerical tool [22,23] based on

the Finite Volume method (FV) to solve the system of non-linear Shallow Water Equations (NLSW) modified with non-conservative terms to account for account topo-bathymetric effects, as described in Eq. (7):

$$\begin{cases} \partial t\, h + \partial_x (hu) + \partial_y (hv) = 0 \\ \partial_t (hu) + \partial_x \left(hu^2 + \frac{g}{2} h^2 \right) + \partial_y (huv) = -gh\partial_x b \\ \partial_t (hv) + \partial_x (huv) + \partial_y \left(hu^2 + \frac{g}{2} h^2 \right) = -gh\partial_y b \end{cases} \tag{7}$$

where h is the water depth, u and v are the fluid velocity components in orthogonal directions (x and y directions), b is the bathymetry, g is the gravitational acceleration, and $\partial_{t,x,y}$ are the partial derivatives with respect to time and space in x and y directions, respectively. For the application example in this paper, the bathymetric conditions are prescribed using data downloaded from the General Bathymetric Chart of the Oceans (see Data Availability Statement), complemented with 1 m high-resolution topo-bathymetric data from a digital elevation model of the Sines coast [35]. The validation of the NLSW-FV tool is performed by correlating numerical solutions and data recorded during the 2011 Japan Tsunami. See in Appendix A.2.

The transition from the NLSW-FV domain to the NS-SPH domain is obtained by capturing the hydrodynamic quantities at the VG implemented at the cell that immediately precedes the position that coincides with the location of the open boundary condition used to initiate the NS-SPH domain. The open boundary condition [36] is prescribed by a buffer layer of particles with a chosen width of $6\Delta p$ in the normal direction.

The NS-SPH code used is implemented in open-source DualSPHysics software (version 5.0) [25]. The full description of the Lagrangian-based NS-SPH scheme can be found in DualSPHysics literature [24,25]. A detailed description of the hydrodynamic model based on a coupling technique adopting Dirichlet boundary conditions can be found in Reis et al. [20,21], which also describe calibration and validating of the NS-SPH numerical solutions against experimentally recorded data [37–39]. In modeling critical infrastructure such as the application example in this paper, the topo-bathymetric conditions are assigned to the NS-SPH model based on average approximations of the high-resolution grids, from which transverse profiles every 100 m in the longitudinal direction (perpendicular to shoreline) were extracted. The domain was set to cover the average limit of tsunami inundated area given by the NLSW-FV solution (≈1.5 km). The topo-bathymetry and the infrastructure system are first geometrically modeled using Blender [31], which is an open-source rendering engine capable of exporting .stl format files, which are then imported by the NS-SPH code.

The NS-SPH code numerically solves the Lagrangian system of NS equations for weakly compressible fluids complemented by Tait's state equation in the form of Eq. (8) reads:

$$\begin{cases} \frac{dV}{dt} = -\frac{1}{\rho} \nabla p + g + \Gamma \\ \frac{dr}{dt} = V \\ \frac{d\rho}{dt} = -\rho \nabla V \\ P = \beta \left[\left(\frac{\rho}{\rho_0} \right)^{\gamma} - 1 \right] \end{cases} \tag{8}$$

where $V = (u, v, w)^T$ is the velocity field, t is the time, p and ρ are pressure and density, respectively, g is the gravitational acceleration, r is the position, and Γ represents the dissipative term. In Tait's equation, density and pressure are related assuming the reference density ρ_0 equals the gas density at rest, while parameter $\gamma = 7$ is the polytrophic constant and $\beta = \rho_0 C_s^2/\gamma$, where C_s is the speed of sound.

The SPH method substitutes the continuum properties of the fluid by a set of discrete interacting particles, which are defined by fluid properties (density, velocity, pressure). Each particle is related to neighboring particles by means of a kernel function W that mimics the integro-differential operators. Any function, f, that is dependent on the particle position vector, r, is approximated through the integration of the relevant properties of all the particles that lie within the radius of the smoothing length given by Eq. (9):

$$\langle f(r) \rangle = \int_{\Omega} f(r') W(r - r', h_{sph}) dr' \tag{9}$$

where $W(r - r')$ is the kernel, h_{sph} the smoothing length defining the radius of influence of domain Ω and $\langle ... \rangle$ an approximation operator.

Considering a discrete particle set, Eq. (9) is substituted by a discrete summation over all the particles inside the kernel. Consequently, for any particle a with position $r_a = r_a(t)$, the discrete average is given by Eq. (10):

$$f(r_a) = \sum_{b \in N(a)} f(r_b) \frac{m_b}{\rho_b} W(r_a - r_b, h_{sph}) \tag{10}$$

where m is the mass and b stands for the particles that belong to the discrete kernel support of particle a, $N(a)$. Integrating Eq. (8) by parts, using the divergence theorem, and assuming that the kernel support is compact, the derivatives are supported by the kernel

function and the conservation equations of momentum and mass continuity, complemented by Tait's state equation, are then given by Eq. (11):

$$\begin{cases} \dfrac{dv_a}{dt} = -\sum\limits_{b\in N(b)} m_b \left(\dfrac{p_a + p_b}{\rho_a \cdot \rho_b} + \prod\limits_{ab} \right) \nabla_a W_{ab} + g \\ \dfrac{dr_a}{dt} = v_a \\ \dfrac{d\rho_a}{dt} = \sum\limits_{b\in N(b)} m_b v_{ab} \nabla_a W_{ab} \\ P_a = \beta \left[\left(\dfrac{\rho_a}{\rho_0} \right)^{\gamma} - 1 \right] \end{cases} \tag{11}$$

where $\prod$ is an additional artificial viscosity term introduced for the sake of stability of the numerical solutions [40].

The particle impact against a rigid structure is determined by the momentum rate hitting the wall at a discrete time t^n by solving the momentum equation at interpolation distance less than $2h_{sph}$. The computation of the force exerted by the fluid against a solid object at time t^n is then computed as the summation of the momentum variation of each surrounding fluid particle b inside the kernel influencing boundary particle a that is in the neighborhood of the solid and experiencing an acceleration (Eq. (12)):

$$F = \sum_{b\in 2h_{sph}} m_b \left(\frac{dv_{ab}}{dt} \right) \tag{12}$$

where m_b is the mass of particle b and $\frac{dv_{ab}}{dt}$ is the difference in acceleration between particles a and b. Note that the summation is only carried out for the particles that hit the surface of the solid in the time interval $[t^n, t^{n+1}]$.

3. Port of Sines case study

The strategic location of Portugal is unique, both in the North-South Atlantic interconnection (with access to Africa and South America), East-West (access to North America), to Europe itself and to the Mediterranean Basin, and through the latter, to the Middle East and Asia (see Fig. 2). In 1978, restrict-less maritime access and the natural conditions of the region contributed to make the decision of implementing a modern deep-water seaport in Sines. The Sines port became the main port in the Iberian-Atlantic front, representing the leading energy supplier (crude, refined products, and natural gas), as well as an international structure on the maritime traffic of containerized cargo [41]. An 8 billion Euros public investment is currently commissioned to take advantage of the region's growth potential by expanding the gas and container hub of the port complex, implementing deep-sea mooring and landing of fiber optic submarine cables and respective mega data centers, and enhancing maritime and hinterland connections [42]. Moreover, some of the port structures, such as the container terminal, also play an important lifeline role in the case of emergency response, all of which contribute to its critical nature when assigning a design level of importance and respective performance requirements [13]. The Sines −28 m ZH container terminal, Terminal XXI, consists of a closed typology 300 m-long gravity caisson block quay and an open typology 700 m-long quay supported by alternating alignments of two and five piles, spaced 6 m on-center in the perpendicular to the shoreline direction (designated as longitudinal direction "L") and ranging 4 m to 9.5 m on-center in the parallel to shoreline direction (designated as transverse direction "T"), as shown in Fig. 3.

The high concentration of the critical infrastructure implemented in the coastal region constitutes a development opportunity as well as an engineering challenge. The North East Atlantic and Mediterranean (NEAM) coastline regions are susceptible to major tsunamigenic earthquakes, such as the 1755 Great Lisbon Earthquake and Tsunami (GLET). The 1755 GLET event has such historical importance that it is the reference for an extreme earthquake and tsunami events in the Atlantic waterfronts of Europe and Morocco [43,44], and is therefore used to define the seismic hazard the current design codes of the built infrastructure located in the NE Atlantic and Mediterranean regions.

For the 1755 GLET historic event, multiple fault locations and rupture parameters have been proposed in the literature [44–51]. However, due to the complex systems of geological structures in the NEAM region [52], the most likely source of the 1755 historic event remains a topic of debate in the scientific community. Moreover, due to the infrequent nature of such extreme events in the NEAM region, the propagation and arrival of the seismic and tsunami waves constitute another source of great uncertainty that must be properly accounted for when studying critical infrastructure systems, such as the Port of Sines.

To study the cascading earthquake and tsunami (ET) hazards and their impact on the Port of Sines, Reis et al. [5] used 36 different tsunamigenic earthquake sources that could have given rise to the 1755 ET event with assumed fault parameters obtained from the literature. For each of the 36 sources, 24 different GMPEs and four different coastal topo-bathymetric configurations (accounting for possible future expansions of the Port of Sines) were assessed. To provide some an idea of the data generated in Reis et al. [5], the left subplot in Fig. 4 shows all earthquake and tsunami peak intensity measures assessed for nine tsunamigenic sources, including the peak ground acceleration (PGA), the free surface elevation measured relative to zH (η), and the peak moment flux (M_f). Positive *eta* values represent the inflow of water and increased inundation depth, while negative *eta* values represent water outflow. Note that each source produces one unique momentum flux and *eta* pair and that the multiple points in the figure per momentum flux and *eta* pair are due to the 24 GMPEs used, which cause a significant spread in the seismic ground shaking PGA intensity measure. Such a large spread in the PGA values is associated with the lack of regional historical data to calibrate the GMPE scaling with magnitude, distance, and period of large magnitude events, such as the 1755 GLET and the large number of plausible

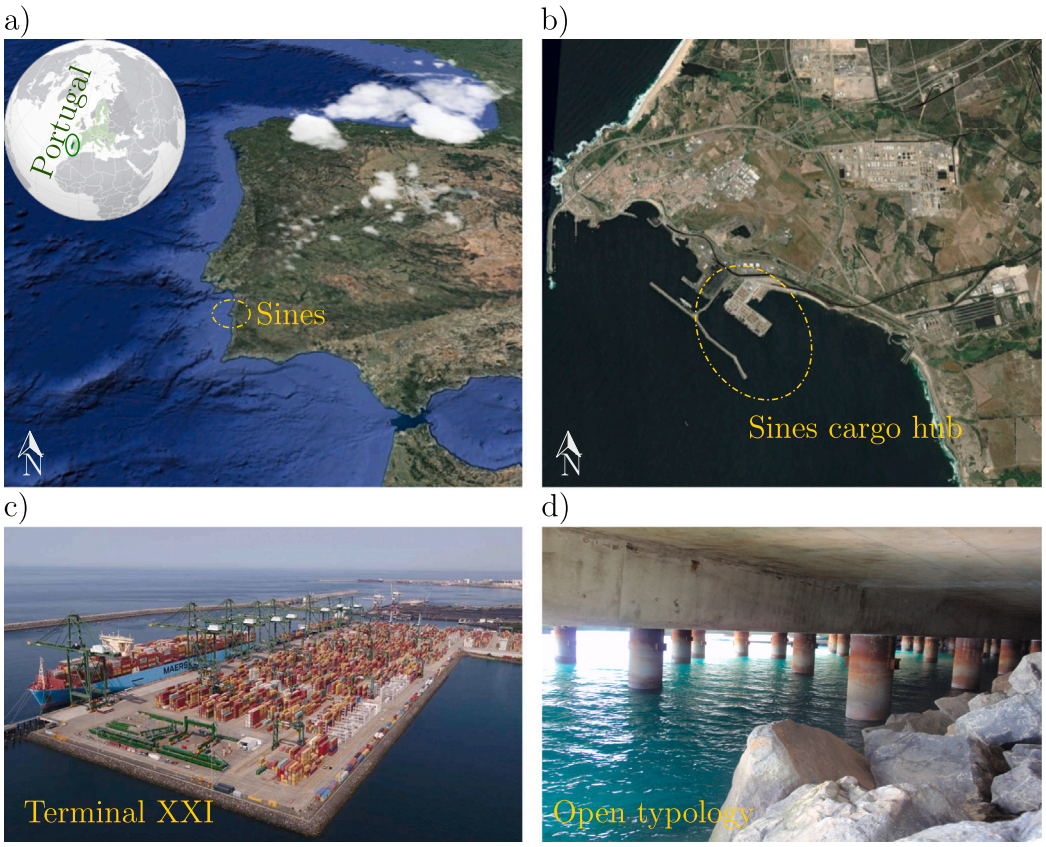

Fig. 2. Port of Sines case study: (a) location of Portugal and Sines, (b) location of the deep-water seaport in the Sines region and position of the container terminal in the port complex, (c) digital image of Terminal XXI (view from the East), (d) digital image of Terminal XXI (view from above).

scenarios considered. In Reis et al. [5], the PGA values were correlated to PGA values derived from the macro-seismic intensity maps and design recommendations adopted from Eurocode 8 Portuguese National Annex for class IV infrastructure considering a type 1 (far-field) event with return periods of one in 1303-years. In Reis et al. the PGA values were correlated to PGA values derived from the macro-seismic intensity maps and design recommendations adopted in the Eurocode 8 Portuguese National Annex for class IV infrastructure considering a type 1 (far-field) event with a return period of one in 1303-years. Although the class of structures is defined up to class IV, the Eurocodes define the minimum values that should be considered in the design, but do for the consideration of larger return periods for critical structures that fall outside the scope four classes of importance defined in the Eurocodes. Thus, the PGA value of a Mw 8.7 scenario corresponding to a 1755-alike GLET was calculated based on a one in 3000-years return period as suggested in Matias et al. 2013 [50]. The results of this correlation indicated that the Atkinson and Boore [53] GMPE provided a reasonable and reliable model for the 1755 GLET, even when considering such varying scenarios as indicated in Fig. 4. Figs. 4(b) to 4(d) show the scatter plots of the ground shaking and tsunami intensity measures, considering the various fault source scenarios and the Atkinson and Boore [53] GMPE. Interestingly, and not previously reported in Reis et al. Figs. 4(b) to 4(d) show positive linear correlation trends, even though PGA values greater than 0.352 g heavily influence the correlation coefficients, as through comparison indicated in Tables 1 and 2. Considering PGA value as leading variable, the highest correlation coefficients are $\rho_{\eta,M_f} = 0.755$ $\rho_{M_f,PGA} = 0.730$, but if PGA values greater than to 0.352 g are excluded, the correlations drop to $\rho_{\eta,M_f|PGA<0.352\,g} = 0.495$, $\rho_{M_f,PGA|PGA<0.352\,g} = 0.13$.Various transformations of the IMs were considered and it is worth noting that the largest correlation coefficient was estimated as $\rho_{ln(M_f),ln(PGA)} = 0.875$.

In this paper, we consider a few of the tsunamigenic scenarios shown in Fig. 4 to illustrate the numerical methodology described above to generate consistent earthquake and tsunami simulations. The genesis of the event corresponding to each seismic and tsunami scenario is defined in terms of geometric, kinematic, and geotechnical parameters, which are summarized in Table 3, which are used to set the initial conditions of the seismic and tsunami simulations.

3.1. Seismic ground shaking simulations

Besides the fault rupture parameters listed in Table 3, EXSIM [19] requires additional inputs, including stress drop, type of fault, $stress_{ref}$, hypocenter location and down dip distance from the fault, geometric spreading, quality factor, damping of response spectra,

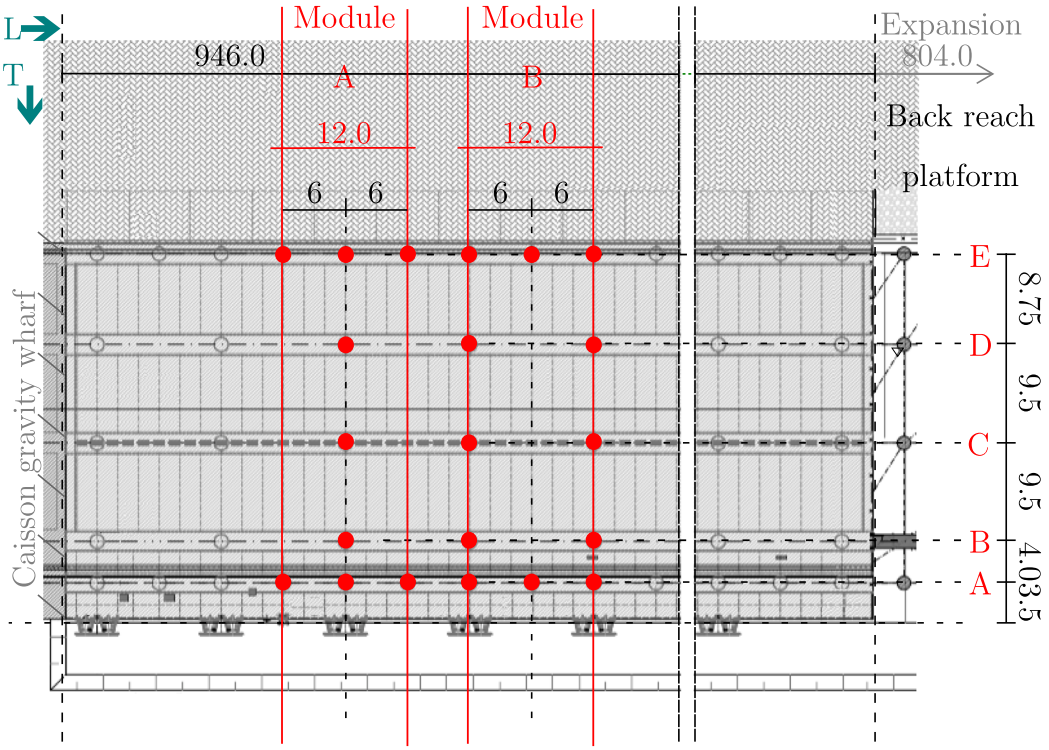

(a) Plan view of the container terminal pile-supported quay.

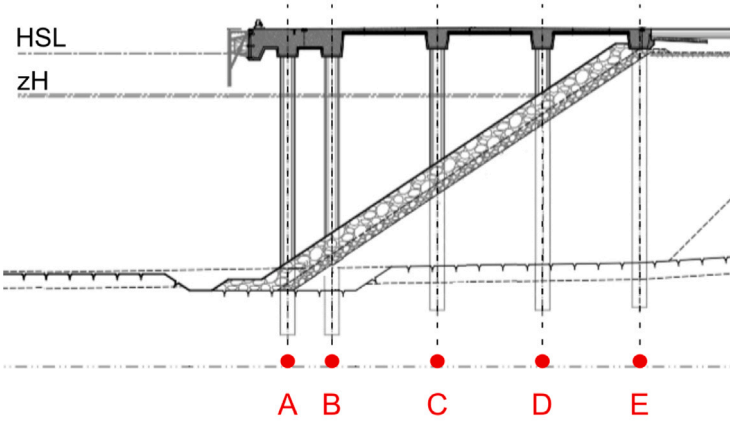

(b) Transverse profile of the pile-supported quay.

Fig. 3. Structural dimensions of the open typology section of the container terminal. The 12 m strips (in red) correspond to the sections discretized in detailed in the NS-SPH simulations described below. (For interpretation of the references to color in this figure legend, the reader is referred to the web version of this article.)

number of frequencies, frequencies, crustal amplification filter for frequencies, site amplification for frequencies, slip weight for sub-faults, seed and number of trials, as well as the number and location of sites for which ground motion time series are generated.

To define the stress drop, an overall and broad region of the distributed deformation under NNW-SSE compressive stress-fields was reported for Portugal's mainland and adjacent West Iberian region [55–58]. Ribeiro et al. [55] considered a value of 100 bar, indicating that this value was an upper bound for the local stress and considering it to be an overestimation. Zonno et al. [56]

Table 1
Linear correlation matrix of earthquake ground shaking and tsunami flow intensity measures considering all scenarios analyzed.

	η	PM_f	PGA
η	1	0.755	0.738
PM_f	0.755	1	0.731
PGA	0.738	0.731	1

Table 2
Linear correlation matrix of earthquake ground shaking and tsunami flow intensity measures considering scenarios that produced $PGA < 0.352$ g.

	η	PM_f	PGA
η	1	0.495	0.347
PM_f	0.495	1	0.137
PGA	0.347	0.137	1

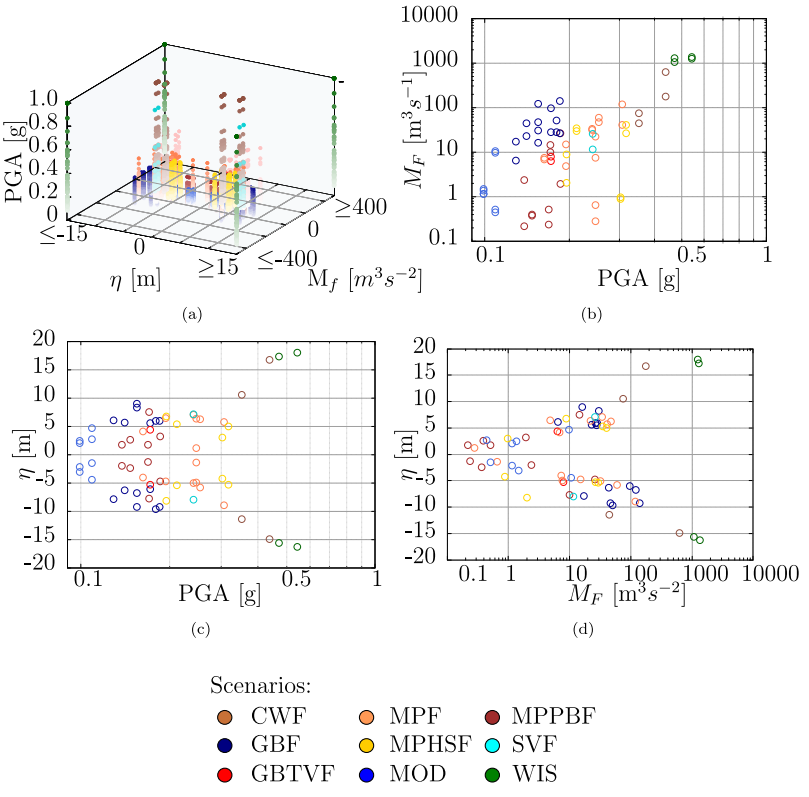

Fig. 4. ET intensity measures for various tsunamigenic scenarios: (a) Three-dimensional plot of the ground shaking intensity measure, PGA, versus the tsunami free surface elevation η and momentum flux M_F, (b) PGA versus peak M_F, (c) PGA versus peak η, and (d) peak M_F versus peak η. Legend: CWF — Cadiz Wedge fault, MPF — Marquês de Pombal fault, MPPBF — Marquês de Pombal and Portimão Bank faults, GBF — Gorringe Bank fault, MPHSF — Marquês de Pombal and Horseshoe faults, SVF — São Vicente fault, GBFVF — Gorringe Bank and Lower Tagus faults, MOD — Thrust-Wrench interference at southwest Iberia between Eurasian-African plates and Horseshoe faults linked by a corner fault, and WIS — Western Iberian Shelf.

adopted values of 50 bar for offshore sources and 120 bar for onshore seismic sources. Carvalho et al. [57] estimated 101 bar for intraplate and 66 bar for interplate ruptures. Values between 90 bar and 130 bar were later estimated for the Azores region [58]. For the EXSIM simulations, based on this information, a value of 65 bar was adopted as the stress drop parameter due to the interplate nature of the sources that triggered the extreme 1755 event.

EXSIM uses the Wells and Coppersmith relation [59] to relate fault length, width and stress_{ref} when one of the fault dimensions is zero, which is not the case of the modeled faults. Nonetheless, the stress_{ref} value was set as a placeholder to 70 bar, as suggested by EXSIM.

Table 3
Parameters of the thrust fault rupture scenarios: fault geometry (length, L, width, W, and depth to the top, d), kinematics (strike, φ, dip, δ, rake, Θ, and slip, λ), soil rigidity, μ, and moment magnitude, Mw.

Ref.	L [km]	W [km]	d [km]	φ [°]	δ [°]	Θ [°]	λ [m]	μ [10^{20} N m]	Mw
MPPSF - Marquês de Pombal and Pereira de Sousa fault rupture - Terrinha et al.									
[49]	120; 70	100	30; 10	15; 15	9	90	10	3.2	8.6
MPPBF - Marquês de Pombal and Portimão Bank fault - Baptista et al.									
[44]	95; 100	55	17	70; 21.7	45; 24	90	20	3.0	8.7
HSF - Marquês de Pombal - Ribeiro et al.									
[54]	80	175	140	39	45	90	10	6.5	8.7
GBF - Gorringe Bank fault - Grandin et al.									
[46]	170	100	25	60	40	90	13	6.0	8.7

The hypocenter location along the fault and the down dip distance from the fault reference point (an upper corner) were assumed with a random location generated in EXSIM [19].

The geometric spreading was modeled following a bi-linear relationship with the transition at the average value of 34.5 km between 37.5 km given in Zonno et al. [56] and 31.0 km given in Carvalho et al. [57]. The quality factor, $Q = max(Q_{min}; Q_0 F\eta)$, used $Q_0 = 239$ and $\eta = 1.06$ [57,58].

The crustal amplification filter file relating frequency and amplification follows the Atkinson and Boore [60] relationship for hard rock. The site amplification filter considers no amplification for the Port of Sines case study due to its rocky geotechnical conditions.

Non-uniform slip weights were assumed and random values for the weights were assigned to all sub-faults per EXSIM [19].

Given the inherent variability in earthquake ground motions, design standards typically recommend repeating analyses for multiple ground motions to provide statistically robust measures of the demands. Twenty (20) accelerograms were generated for each of the four scenarios. Fig. 5 shows the time series of seismic acceleration for the various scenarios. Additionally, it correlates the stochastic ground motion model and GMPE-based solutions. For the sake of readability, each accelerogram is represented by the median time-history of all accelerograms and a corresponding standard variation obtained from the synthetic accelerograms representing the larger acceleration magnitudes. Black stars represent PGA values obtained using GMPEs. The peak accelerations estimated from the time series, PGA_{TS} are in agreement with the PGA values estimated using the GMPEs, PGA_{GMPEs}, although the PGA_{TS} values tend to overshoot the PGA_{GMPE} values. Differences are likely related with the differences in the modeling approach, including the larger number of parameters considered when defining the stochastic ground motion model in EXSIM.

Fig. 6 shows the mean 5% damped linear-elastic response spectra of the 20 generated acceleration time series and the 5% damped linear-elastic of the EC8 response spectra for the site, considering soil type B. The response spectra corresponding to composite fault ruptures scenarios, such as MPPSF [49] and MPPBF [44] exceeded the EC8 response spectra at both short and long periods. The GBF [46] and HSF [54] response spectra are lower than the EC8 spectra. The predominant period for the generated acceleration time series of was evaluated between 0.2 s and 0.4 s, which indicates the presence of relatively high-frequency content.

3.2. Tsunami action

The tsunami forces induced by the four earthquake source scenarios were modeled using the coupled NLSW-FV and NS-SPH model. The NLSW-FV code is first employed to carry out the simulations of tsunami propagation and inundation at Port of Sines container terminal. The initial conditions of the models adopt the fault rupture parameters identified in Table 3. Based on the fault parameters, the co-seismic vertical displacement is calculated using Mirone software [34], which adopts Okada's half-space theory [33]. The NLSW-FV simulations run over a 4-nested grid with 1:4 ratio of discretization, with the largest being the GEBCO 15 arc-sec grid and the smallest being complemented by a 1 m high-resolution digital elevation model, DEM, for characterization of local effects [35]. The total duration of the tsunami being simulated is set to $t = 7200$ s.

Fig. 7 shows example results of the NLSW-FV simulation for time instants corresponding to maxima free-surface elevation (MPPBF scenario) and peak momentum flux during inflow (HSF scenario) and peak momentum flux during the outflow (GBF scenario) obtained at the multiple VGs implemented along the vicinity of the container terminal. The numerical solutions need an additional disclaimer regarding the importance of considering hydrostatic (free surface elevation) and hydrodynamic (momentum flux) tsunami quantities. The time when the peak of these quantities occur may not be coincident with the first wave of the tsunami, highlighting the importance of considering the tsunami as a time-dependent train of waves when assessing the tsunami effects on coastal infrastructure.

The forces exerted on the container terminal are computed via the NS-SPH code. The domain boundary between NLSW-FV and the NS-SPH models, where the coupling between the two models occurs, are set using free-surface elevation and flow velocity quantities captured at VG_A at the cell that immediately precedes the position of the domain boundary. The local water depth considering mean-sea level condition is set to 0 m. Note that a new axis y is created and referenced to the mean-sea level at $y = 0$ to describe additional details about the model. The distance between the breakwater and the quay is about 850 m while the inundated area extends between $x = 0$ m and $x = 1250$ m, in prototype-scale. In the NS-SPH model, the buffer layer of particles has a width of $6\Delta p$ in the normal direction of model coupling domain boundary (at $x = 800$ m and $y = -23.5$ m). The inlet-outlet configuration is set to convert new particles into fluid particles while allowing reverse flow to mimic tsunami wave outflow in the seaward direction.

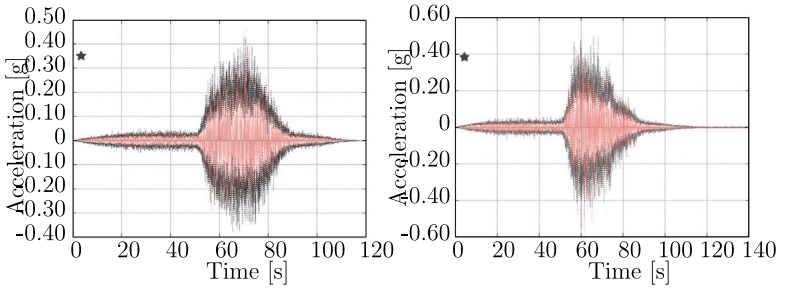

(a) Marquês de Pombal and Portimão Bank (MPPBF) source proposed in Baptista et al. [44] (left) and Marquês de Pombal and Pereira de Sousa (MPPSF) source proposed in Terrinha et al. [49] (right).

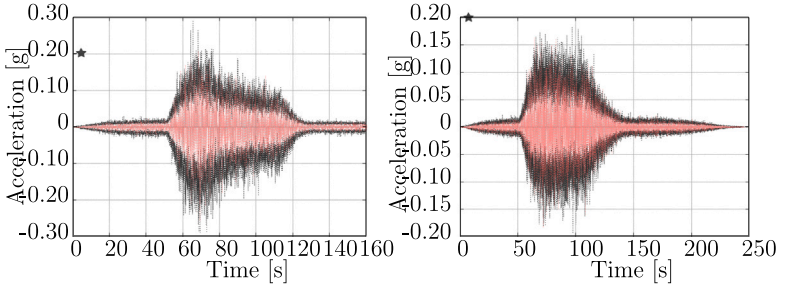

(b) Horseshoe (HSF) source proposed in Ribeiro et al. [54] (left) and Gorringe Bank (GBF) source proposed in Grandin et al. [46] (right).

Fig. 5. Time series of seismic acceleration derived from various scenarios. Red solid lines represent median value and black dotted lines represent standard deviation from the accelerogram with larger accelerations. Black stars represent PGA values obtained using GMPEs. (For interpretation of the references to color in this figure legend, the reader is referred to the web version of this article.)

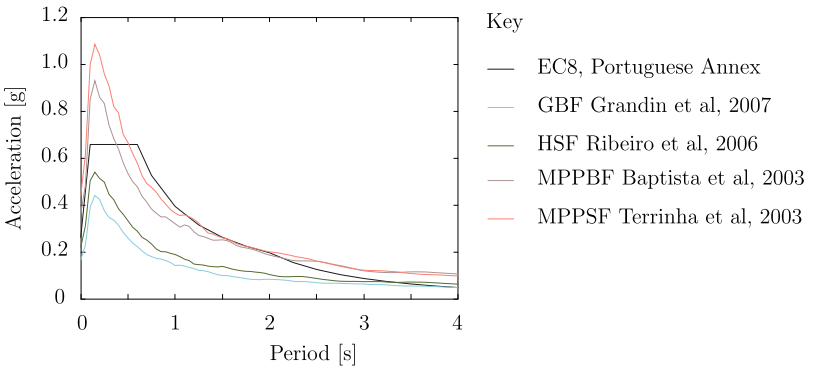

Fig. 6. Five-percent linearly damped elastic response spectrum recommended by the Portuguese National Annex of EC8 (black line) and mean five-percent linearly damped elastic response spectra based on 20 synthetic accelerograms generated using EXSIM (color lines). (For interpretation of the references to color in this figure legend, the reader is referred to the web version of this article.)

Note that for the sake of the computing time needed to obtain the numerical solutions, a reduced-scale model of the prototype of the cargo/shipping hub was simulated in the NS-SPH model. The use of reduced-scale models is an approach that is common in SPH simulations to reduce the computational time. This approach was also used in validation example shown in Appendix. The reduced-scale model used a geometrical scale of $1 : 10$ and a temporal scale of $1 : 10^{1/2}$, based on the Froude similitude using Buckingham's theorem [61,62]. For example, a wave with a free surface elevation of $\eta = 8\,\mathrm{m}$ and period of $T = 12\,\mathrm{s}$ in the real prototype-scale would correspond to $\eta = 0.8\,\mathrm{m}$ and $T = 3.80\,\mathrm{s}$ when converted to the reduced-scale model. The simulations were carried out for intervals of time corresponding to the reduced-temporal scale of the tsunami $t = 2280\,\mathrm{s} \approx 7200\,\mathrm{s}/10^{1/2}$. Note that effects of scour, air entrapment between the fluid and the soffit of the quay slab, and debris impact and damming were neglected in the present study.

A convergence analysis of the NS-SPH models was performed using representative boundary conditions with initial flow depth of $\eta = 1.0\,\mathrm{m}$ and constant flow velocity of $u = 1.6\ \mathrm{m/s^2}$ at the reduced-scale, corresponding to $\eta = 10.0\,\mathrm{m}$ and $u = 5.0\ \mathrm{m/s^2}$ at prototype-scale. The values of $\frac{h}{\Delta p}$ were varied in the range of 20 to 50. The range was selected as a function of the potential wave

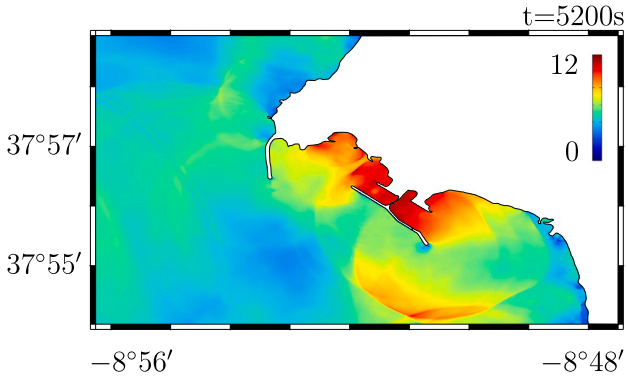

(a) Maximum inundation depth (units: m).

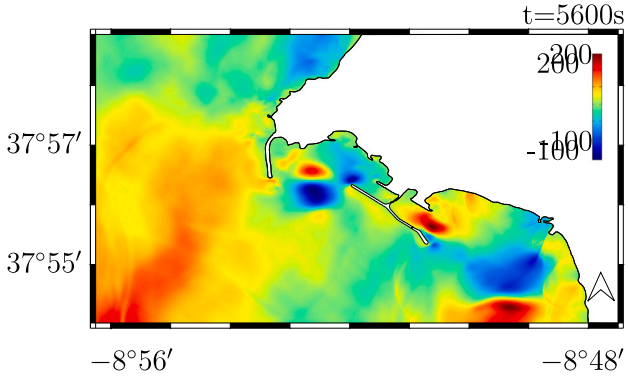

(b) Peak momentum flux during inflow (units: $m^3\,s^{-2}$).

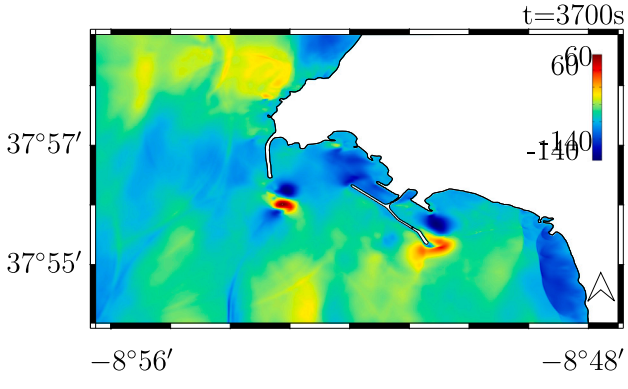

(c) Peak momentum flux during outflow (units: $m^3\,s^{-2}$).

Fig. 7. NLSW-FV results for the four earthquake source listed in Table 3 for instants corresponding to maximum inundation depth η, peak momentum flux during inflow M_F^+ and outflow M_F^-.

characteristics and in accordance with other literature for unbreaking and breaking waves [20,21,63–65]. For the 3D model, a discretization of $\Delta p = 0.2$ m lead to convergence of the free surface elevation results, resulting in more than 4.2 million initial particles and near 124 h of GPU simulation run-time per run using a single graphics processing unit, GPU, Compute Unified Device Architecture, CUDA, driver version 11, 64 CUDA cores per 30 multiprocessors, card NVIDIA GeForce RTX 2060, 2.6 GHz, with 2 GB of memory.

Fig. 8 shows the 3D NS-SPH flow velocity results for the GBF scenario at different times. At instant t_1, the wave generated after the breakwater arrives at the quay immediately occupying the space between the free-surface elevation and the soffit of the quay slab due to the combination of the flow current and the sloping grade of the embankment. The wave propagating towards the quay's frontal 2.5 m-high docking region induces a seaward reflection effect. In addition, the flow velocity behind the terminal is still zero, as the tsunami had not yet reached the back of the terminal. At instant t_2, the increasing pressure and reflection effects become more

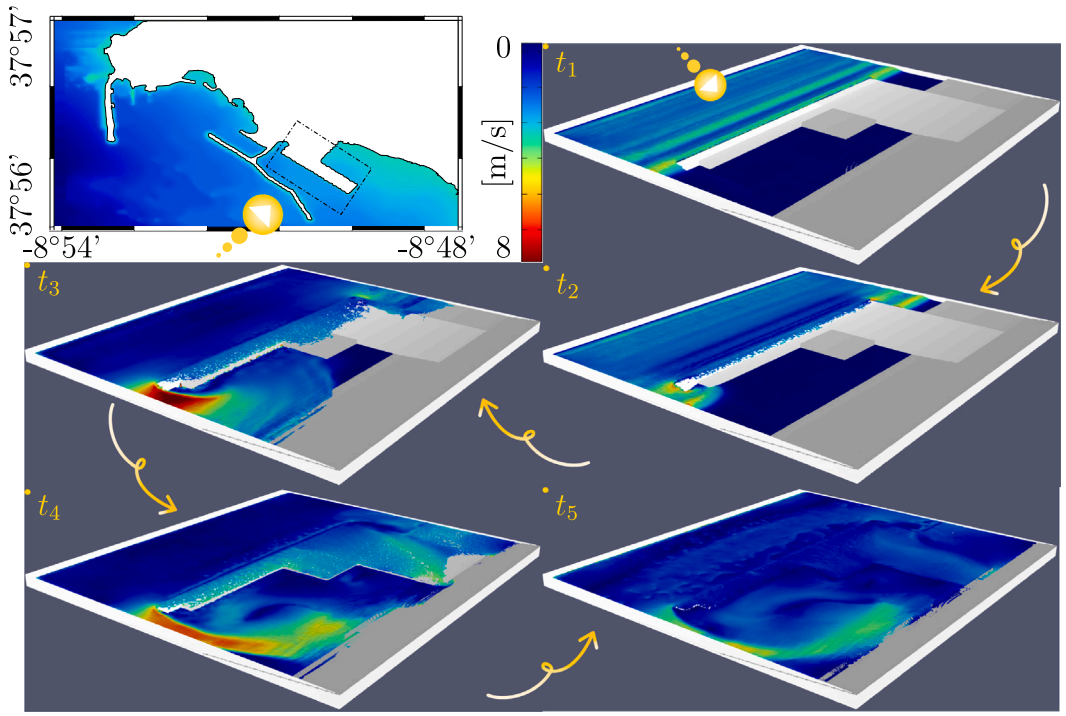

Fig. 8. Dynamic tsunami action: identification of the 3D NS-SPH domain (left) and solution showing the instantaneous particle velocity of the three-dimensional NS-SPH simulation of tsunami arrival at the container terminal considering GBF representative scenario (right).

evident when observing the non-zero velocity wavefront. The flow surrounding the structure has a more accentuated response, with larger velocities. At instant t_3, the high flow velocities near the quay ends are discernible. These high flow velocities are due to both the drag and channeling effects, potentially due to the relatively narrow distance between the quay and model boundary. To ensure the NS-SPH domain boundary was reasonably set, the NS-SPH results were compared with the NLSW-FV results that were computed over a wider domain; from the comparison, it was possible to confirm that similar local velocity amplifications were observed. In the closed typology wharf section, the impact of the flow occurred against the frontal surface perpendicular to the tsunami but the inundation of the quay started from the side, partly due to reflections of the wave and partly due the flow circumventing the higher wharf along the coastline. At instant t_4, the tsunami bore at the quay is starting to overtop the whole quay, while the long tsunami wave keeps being compressed against the structure and the sloping shoreline. At instant t_5, the shipping and storage areas are totally submerged. At this instant, the flow is about to transition from tsunami inflow to tsunami outflow, and the flow currents developed behind the quay are clearly noticeable.

To quantify the tsunami forces, bearing in mind the computational costs of 3D and 2D simulations, a cost–benefit analysis was performed to evaluate the pros and cons of having local three-dimensional effects (full 3D model) or pursuing simulations with more detailed geometry in 2D representations. The 2D model was discretized with $\Delta p = 0.05$ m resulting in 58 thousand initial particles and simulation run-time of about 1 h. However, if considering the possible transverse views of 2D models, it is observed that models of both 5-piles and 2-piles profiles (Fig. 3) limit the assessment of tsunami forces after the first pile, whereas the built-in assessment of tsunami forces in the horizontal direction is limited if considering a fully open 2D model while leading to overestimation of tsunami forces exerted on the vertical direction. Thus, two intermediate 12 m-width pseudo-3D models of the 3D prototype of the container terminal were created, based on dimensions indicated in Fig. 3. The uniformity of tsunami flow impacting the quay along the longitudinal direction (parallel to shoreline) contributed to assuming two pseudo-3D models (a compromise between 3D and 2D models) that repeat themselves along the longitudinal direction of the wharf as Modules A and B, both structurally and in terms of flow conditions. The modules mimic the 2-5-2 and 5-2-5 piles distribution, allowing for the characterization of the tsunami forces exerted on the horizontal and vertical components of the container terminal.

Considering the sensitive nature of the SPH models to user-defined parameters and the absence of data to perform modeling calibration and validation, the numerical solutions were correlated with the results obtained using analytical force equations and flow metrics obtained using the NLSW-FV tool at VG_B, which is located at 1 m from the container terminal. The comparison is performed for $t \approx 650$ s in the reduced-scale model, i.e. $t \approx 2200$ s in prototype-scale, as represented in Fig. 8. Fig. 9 shows the correlation of horizontal tsunami forces exerted on the pile supported quay considering the representative GBF scenario. The correlation of the tsunami forces is conducted only during the arrival of the first wave, avoiding the influence of more complex hydraulic phenomena after the impact against the elevated structure, to allow for a reasonable comparison between modeling

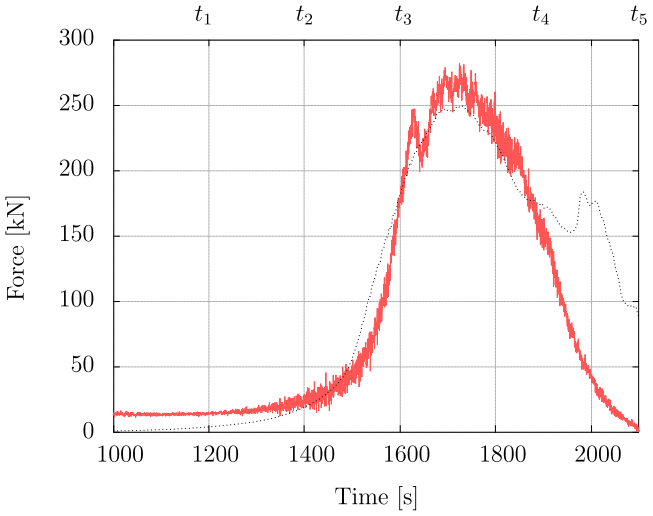

Fig. 9. Tsunami loading on a pile. Red solid lines represent force solution calculated via the NS-SPH model and black dotted lines represent the semi-analytical solution with hydrodynamic quantities obtained via the NLSW-FV simulations.

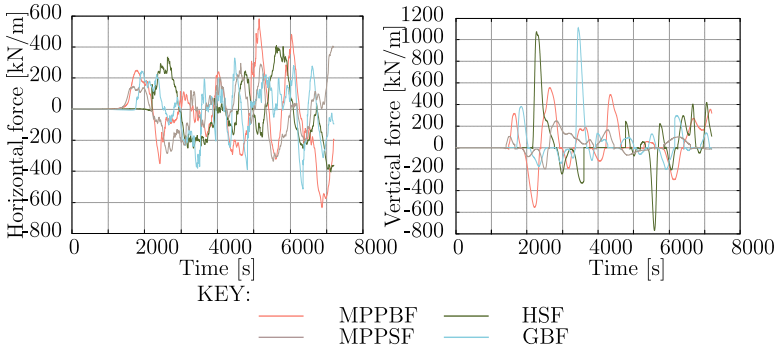

Fig. 10. Time-histories of tsunami force on the horizontal (left) and vertical (right) directions derived from the various scenarios.

approaches. It can be seen that the NLSW-FV model overestimates the first wave reflection when compared to the NS-SPH solution. The differences observed in the correlation of the two solutions are likely related with the basis of the numerical formulations. For the NLSW-FV numerical scheme, the quay is a full obstacle to the flow, while for the NS-SPH scheme the geometry of quay represents a partial obstacle to the tsunami flow.

Fig. 10 shows the time-histories of tsunami horizontal and vertical forces obtained from the MPPBF, MPPSF, HSF, and the GBF scenarios. On the horizontal direction, positive forces represent the fluid pushing the structure from the sea- to land-ward direction. On the vertical direction, positive forces represent tsunami uplifting effects.

3.3. Dynamic loading patterns

Example time series of seismic acceleration and tsunami forces in horizontal and vertical directions are shown in Figs. 5 and 10, respectively. The seismic acceleration and tsunami force time series shown are for the MPPBF, MPPSF, HSF, and GBF scenarios. Fig. 11 provides a schematic representation of the loading patterns and their points of application. Earthquake accelerations are to applied at the bed-rock level while tsunami forces would be applied as uniformly distributed forces on the structural elements.

The ratio between horizontal and vertical forces vary up to 70% in some instants of the time series of the tsunami forces exerted on the pile-supported quay. For the different scenarios the maximum difference is observed during the peak of the first (e.g. GBF scenario) and the third (e.g. GBF scenario) waves during inflow stages.

The uncertainty about the most suitable distribution pattern for the representation of the hydrodynamic forces remains in the literature [66], varying among triangular and trapezoidal patterns or different distribution patterns [67] and modified Goda equations [68]. Although the solutions obtained via pseudo-3D models represent a compromise between full 3D models and 2D models, preliminary insights on the distribution of the forces can be inferred from the numerical solutions. The horizontal component of the tsunami force exerted on the piles presented a relatively uniform distribution. In addition, it is worth noting that shielding

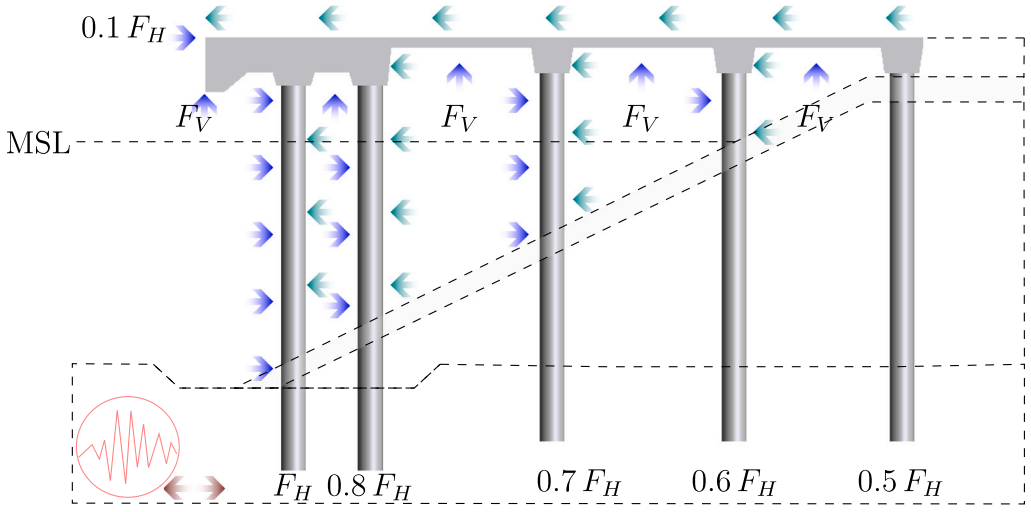

Fig. 11. Loading scenarios generated. The seismic acceleration imposed at the bed-rock level (red), tsunami pressures during inflow stage (blue) and tsunami pressures during outflow stage (green). (For interpretation of the references to color in this figure legend, the reader is referred to the web version of this article.)

effects were clearly observed; the ratio of the value of the uniformly distributed load applied to each pile to the value of the uniformly distributed load applied to seaward facing pile was 100% for the first pile, 80% for the second pile, and consecutive reductions of 10% for each back piles. Numerical solutions also highlighted that tangential forces on the quay during inflow and outflow represent less than 10% of the horizontal loads exerted to the piles.

In the vertical direction, a linearization of the highly non-linear phenomena occurring under the quay was adopted to define the uniformly distributed tsunami uplifting force. The assumption of simplifying the geometry (regular soffit of the quay) and neglecting multi-phase phenomena may represent an over-simplification of the tsunami pressure distribution. Yet, for the tsunami force it is a reasonable approach for designing the specific structural system of a pile-supported quay with circa 1 km-length and a reduced volume of air between the water free surface elevation and the soffit of the less than 40 m quay slab (Fig. 3). The large-scale geometry of the wharf system and ratio between the ≈1 km-longitudinal and ≈40 m-transverse dimensions prevents the tsunami to flow laterally. Such effects lead to a rapid inundation of the space below the quay that starts behaving like a full box. The tsunami long-wave(s) then starts inducing an uniformly distributed compression transmitted to the quay via a simple triangular decomposition of the force obtained from the hydrodynamic quantities encountering the seaward edge of quay as a wall, as assumed on the quantification of forces obtained using the semi-analytical approach that employ flow values obtained using the NLSW-FV simulations.

Future work considering the irregular geometry of the soffit of the quay would provide additional insights on tsunami pressure exerted during inflow (uplift) and outflow (suction effects), as well as influencing parameters such as multi-phase phenomena due to air entrapped under the quay slabs.

4. Conclusion

A numerical methodology was presented to generate consistent earthquake ground shaking accelerations and tsunami forces targeting critical infrastructure. The methodology was validated by comparing results from the numerical modeling approach with field data from 2011 Japan Earthquake and Tsunami (see Appendix). The methodology was then applied in a case study of the container terminal of the Port of Sines using selected historic tsunamigenic earthquake scenarios off the coast of Portugal. The earthquake ground motion acceleration time series were generated using EXSIM with inputs for four scenario earthquake source and source-to-site parameters that were collected from the literature to illustrate the input and outputs of the method. The tsunami forces were determined using consistent earthquake source parameters. Based on the consistent source parameters, the propagation and inundation of the tsunami was modeled using a nonlinear shallow wave equation finite volume (NLSW-FV) code up to a series of virtual gauges near the port infrastructure. The flow depth and velocity outputs at the virtual gauges, VG, served as input conditions to the a Navier–Stokes Smooth Particle Hydrodynamics model, which along with a rigid model of the container terminal of the Port were used to simulate the tsunami forces do to the inflow and outflow tsunamis generated for each of the four scenarios.

The main findings of the study are:

- The median ground motion acceleration time series generated contained peak acceleration values that exceed estimates obtained using GMPEs with similar source parameters in [5];

- The response spectra derived from the acceleration time series show that the GBF and HSF scenarios produce smaller spectral acceleration values when compared to the EC8 design response spectra (Portuguese Annex of Eurocode 8). The MPPSF scenario, and to a lesser extent the MPPBF scenario, produces spectral accelerations that are very close to the EC8 design response spectra, except for the of shorter periods where both the MPPSF and MPPBF scenarios exceed the EC8 design response spectra;
- The forces exerted on the pile-supported quay were computed using a built-in algorithm implemented in the NS-SPH code. The time series show maxima values of $F_h \approx 400\,\mathrm{kN/m}$ and $F_v \approx 1000\,\mathrm{kN/m}$, exceeding the previous estimates adopting a baseline approach, which translates to a $\frac{F_v}{F_h} \approx 2.5$. In some instants of the time series of horizontal and vertical tsunami forces exerted on the pile-supported quay, the forces vary up to $\frac{F_h}{F_v} \approx 70\%$.
- Due to complex hydrodynamic phenomena under the quay slab, the SPH method was the only way to reliably estimate these forces as currently there are no code provisions or documents available in the literature for estimating tsunami forces applied to wharves with open typology, which are characteristically different from other elevated structures due to the embankment limiting the tsunami flow.
  Based on the results of the pseudo-3D modeling performed:
  - the pressure distribution for horizontal forces exerted on the piles highlighted shielding effects due to piles spacing and distribution. In the quay, the tangential component is circa 10% of the perpendicular component of the tsunami horizontal force,
  - a uniform pressure distribution for vertical forces for use in design was proposed due to rapid inundation of the space below a large-scale structure (about $1\,\mathrm{km}$) that prevents outflow and quickly behaves like a block to the tsunami long wave during inflow. Note, however, future work should consider additional phenomena such as that due to compression and suction of air entrapped under elevated structures with irregular geometry, namely the soffit of the quay and the irregular surface of the embankment with varying slope angles,
- Tsunami engineering for elevated structures, and ports in particular, would benefit from future research into tsunami pressure distribution. In the horizontal direction, it would be worthwhile to assess the effects of spacing among the group of piles, i.e., distance between piles affecting drag forces. In the vertical direction, irregular geometry of the soffit of the slabs, multi-phase phenomena due to air entrapped under the quay and embankment slopes may influence tsunami pressures during inflow (uplift) and outflow (suction effects). Understanding the effects of scouring of the foundations due to tsunami flow during run-up and draw-down would also benefit from further research. For the case-study, the study of a potential retrofit of the port of Sines terminal or possible design of future infrastructure in the Sines cargo hub would benefit from conducting nonlinear dynamic structural response analysis considering time-dependent cascading ground motions and tsunami loading. The seismic actions used in this case study exceed the design seismic action for a Eurocode structure class III, while the tsunami loading have not yet been considered in the design processes of the Sines cargo hub. Several aspects of the as-built quay terminal raise concerns that warrant further investigation. For example, the pile-supported quay of the container terminal, only has bottom reinforcement, thus not providing much resistance to uplifting effects, except for their self-weight. The weight of these slabs is about half the peak estimated tsunami forces in the vertical direction, meaning the failure of these structural elements would be eminent in the scenarios considered in this study. Other concerns exist, namely related to the existence of short columns and local deterioration which may also affect the structural capacity. Therefore, detailed structural response analyses would assist in identifying at which stage in the event the Sines cargo hub would become inoperable in the case of an extreme event, such as the 1755-GLET.

CRediT authorship contribution statement

Cláudia Reis: Conceptualization, Formal analysis, Investigation, Methodology, Software, Writing – original draft, Writing – review & editing. **André R. Barbosa:** Formal analysis, Funding acquisition, Writing – review & editing. **Maria Ana Baptista:** Conceptualization. **Mário Lopes:** Writing – review & editing. **Stéphane Clain:** Writing – review & editing.

Declaration of competing interest

The authors declare that they have no known competing financial interests or personal relationships that could have appeared to influence the work reported in this paper.

Data availability

Datasets related to this article can be found at:
• summary of single and composed fault parameters used to model seismic and tsunami source rupture [5]
• summary of attenuation laws for seismic wave propagation at OpenQuake engine library [69]
• topo-bathymetric grids from General Bathymetric Chart of the Oceans
https://www.gebco.net/
• records from Tohoku-Oki, Japan, 2011 tsunami for validation of GMPE solutions from Japan's National Research Institute for Earth Science and Disaster Resilience

https://www.kyoshin.bosai.go.jp/

• records from Tohoku-Oki, Japan, 2011 tsunami for validation of NLSW-FV numerical solutions from NOAA's National Centers for Environmental Information

https://www.ngdc.noaa.gov/

• experimentally acquired data of fluid-structure interactions is available at online DesignSafe repository [37].

Numerical tools related to this article can be found at:

• EXSIM code, 2012 [19]
• Mirone code [34]
• DualSPHysics open-source code [25]
• Blender open-source [31].

Acknowledgments

Lopes and Reis acknowledge the FCT - Fundação para a Ciência e Tecnologia, Portugal support through funding UIDB/04625/2020 from the research unit CERIS. Clain, Baptista and Reis acknowledge the financial support by (1) FEDER - Fundo Europeu de Desenvolvimento Regional, through COMPETE 2020 - Programa Operacional Fatores de Competitividade, and the National Funds through FCT - Fundação para a Ciência e Tecnologia, Portugal, project no. UID/FIS/04650/2019, and (2) FEDER, through COMPETE 2020, and the National Funds through FCT - Fundação para a Ciência e Tecnologia, Portugal, project no. POCI-01-0145-FEDER-028118. The authors acknowledge the support and structural design details provided by Administração dos Portos de Sines e do Algarve, S.A.

Barbosa and Reis would also like to acknowledge funding provided by the US National Science Foundation under grant no. 1661315 which allowed for the initiation of the work. The work was completed with support from US National Science Foundation, United States Award 2103713 and the Center for Risk-Based Community Resilience Planning, United States, which is a NIST-funded Center of Excellence (NIST Financial Assistance Award Numbers: 70NANB15H044 & 70NANB20H008).

The findings and conclusions in the paper are those of the authors and do not necessarily reflect those of the sponsoring agencies.

Appendix. Validation of earthquake and tsunami modeling tools

The 2011 Japan Earthquake and Tsunami was the most recorded event in history. To validate the conceptual methodology for generating cascading earthquake ground motion acceleration time series as well as tsunami flow depths and flow velocities, data recorded by the Japanese National Research Institute for Earth Science and Disaster Resilience (NIED) and tsunami data recorded by the monitoring Buoy Center of the National Oceanic and Atmospheric Administration are used to assess the adequacy and efficiency of the numerical tools and solutions.

Assuming the tsunamigenic source as the cornerstone to conduct scenario-based earthquake and tsunami hazard assessments, the source of the 2011 Japan Earthquake and Tsunami needs to be first characterized. The hypo-center of the Mw 9.1 earthquake was identified off the Sanriku coast, northeast Japan, at geographical latitude and longitude coordinates of 38.1035°N and 142.861°W, and about 15 m in depth. In the literature, multiple finite-fault models were proposed by different authors for the rupture of the reverse fault type with WNW-ESE compression axis that triggered the earthquake and tsunami event [70–74]. While several exist, the Fujii et al. [72] source parameters were selected to generate earthquake and tsunami initial conditions.

The Fujii et al. [72] finite-fault model proposed consists of a source divided into forty 50 km-sided sub-faults for which the focal solution (strike, φ, dip, δ, and rake, Θ) is obtained from the U.S. Geological Survey and the slip, λ, at each sub-fault is estimated from the inversion of tsunami wave-forms recorded at coastal tide gauges, GPS wave gauges and DART stations [23]. Besides kinematic properties, the soil rigidity, μ, is also considered to model the generation phase.

A.1. Earthquake models

The seismic simulations are performed for two of the 1225 records acquired at two stations from K-NET, which include three data channels that correspond to three components of a seismograph, as well Kik-net, which includes six data channels, where the first three correspond to three components of a borehole seismograph and the other three correspond to those of a surface seismograph. Fig. A.12 depicts the locations of IWT023 - Kamaishi station, Iwate prefecture, and IBRH17 - Kasumigaura station, Ibaraki prefecture.

The open-source Open-Quake software [69] is used to determine a map of PGA distribution in part of the Japanese territory during the 2011 event, similar to the methods used in Reis et al. [5] to determine the distribution of PGA in Southwest Portuguese territory. The source modeling assumes a single planar rupture with a middle-top surface aligned with the hypocenter. The fault parameters include a 400 km × 200 km rupture geometry, with $\Theta = 20°$, $\varphi = 30°$, and $\delta = 18°$. A 5 m-resolution grids is defined between longitude 130°W and 150°W, and latitude between 28°N and 43°N. The propagation of the seismic waves was modeled using several attenuation laws developed for the Japanese territory [75–78]. Considering the best fit between recorded and numerical solution, the propagation of seismic waves is modeled using the attenuation law proposed by Abrahamson et al. [76], which was calibrated using data from NGA-West2 database of moderate to large magnitude events that occurred at shallow crust actively tectonic regions and up to 300 km of distance. Site geotechnical conditions are assumed to be stiff soil with a shear wave velocity of the top 30 m $V_{s,30}$ = 760 m/s. Fig. A.12 depicts the correlation between the map of PGA distribution recorded by the Japanese

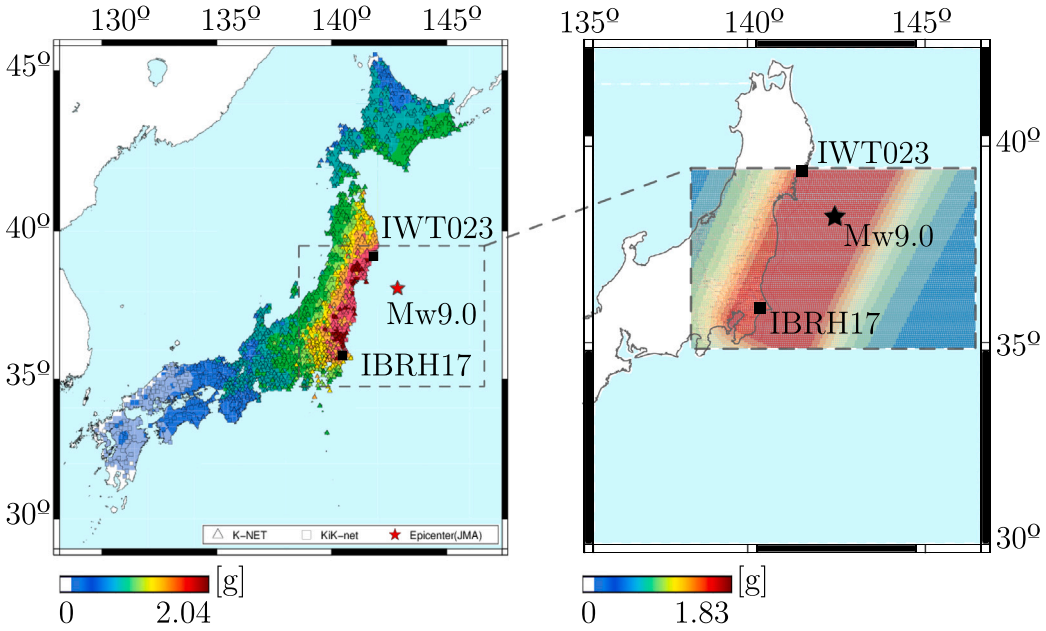

Fig. A.12. Validation of OpenQuake generating maps of distributed peak ground acceleration: correlation between maps of peak accelerations assembled from the records of the Japan strong-motion seismograph networks during the 2011 Japan Earthquake (left), and from PGA data generated using OpenQuake software (right).

seismograph network and the GMPE-based PGA distribution map generated using OpenQuake and the source parameters listed above.

The maps of PGA distribution in the Northeast regions of the Japanese territory demonstrate a general (yet slightly underestimated) agreement between recorded and numerical data. At locations corresponding to IWT023 and IBRH17 stations, the recorded PGA values are 0.42 g and 0.51 g, respectively, while the GMPE generated values are relatively close (≈0.5 g). The differences are likely due to the details in source and site modeling assumptions as well as the assumed GMPE. Attenuation laws developed for Japan subduction systems, with earthquake magnitudes up to $Mw = 9.1$ and distances to the fault less than 300 km are still an active area of research [79]. These could be explored in a future validation study using attenuations laws calibrated from the 2011 extreme event.

The EXSIM algorithm [19] tool is used to develop time series of ground acceleration at the two stations shown in A.12. In the EXSIM model, the same values described above are used for the source geometry (400 km × 150 km), and the following input parameters for the stochastic simulations [80] random slip distribution, 15 MPa of stress drop, 200°-strike, 18°-dip and 18 km-depth. The reference velocity for the bedrock level is taken as 760 m/s, while $k_0 = 0.03$ s. Simulations for the two different sites and twenty trials for each case are performed using the Abrahamson et al. [76] GMPE, with and without site amplification. Fig. A.13 shows the correlation between recorded signals at an Iwate prefecture station, IWT023 - Kamaishi, about 150 km distance from the epicenter, which recorded two distinct phases of strong ground motions and at an Ibaraki prefecture, IBRH17 - Kasumigaura, about 300 km distance from the epicenter and indistinct predominance of phases.

The time series of acceleration also present a relatively accurate (yet slightly underestimated) fitting with the data recorded by the seismic network in terms of wave arrival time and high frequencies, regardless of the Abrahamson et al. scaling law limitations in determining low frequencies [76] (spectral frequencies greater than 1.25 times the high-pass corner frequency used in the record processing, as defined in the NGA-West2 database). The correlation carried out for the IBRH17 station location about 300 km from the epicenter demonstrated a better fitting than the correlation for the closer IWT023 station (about 150 km away from the epicenter). The latter exhibits a two phase, bi-peak ground motion accelerogram, which is difficult to reproduce using a single event with homogeneous slip distribution, while a multiple-event with heterogeneous slip distribution model in the literature [80] was capable of distinguishing the two phases of accelerations. However, the same study [80] assigned the compatibility between recorded and synthetic signals to asperities influencing the radiated waves. Because the distribution of asperities is only known after the event, such a modeling approach is limited to past events.

Lastly, Fig. A.14 depicts the elastic response spectra calculated from recorded and synthetically generated accelerograms for location of the stations at Iwate and baraki prefectures.

The elastic design spectra of the recorded and synthetic signals (at the bedrock) are coherent with the correlations observed in the maps of PGA distribution and time-histories of seismic acceleration for the selected stations. At the IWA23 station location, the correlation between the recorded and the synthetic spectra shows an overestimation of acceleration values during lower periods (T) and an underestimation after $T \approx 0.5$ s, in accordance with the correlation between recorded and generated time-histories of

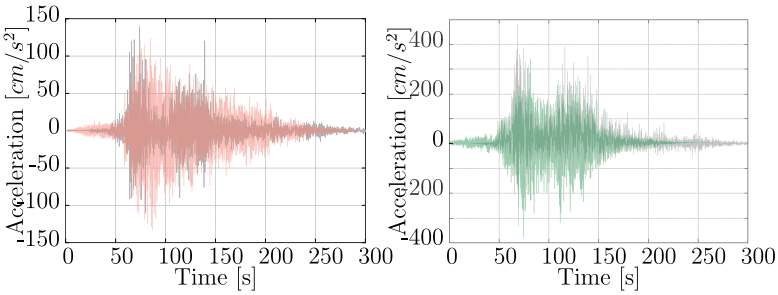

(a) Acceleration at Iwate prefecture, IWT023 - Kamaishi station location, at the borehole (left) and surface (right) levels.

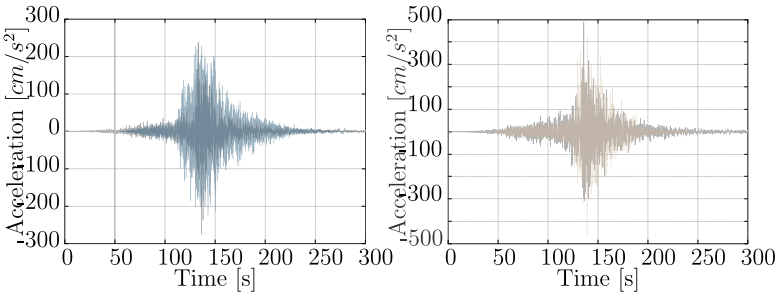

(b) Acceleration at Ibaraki prefecture, IBRH17 - Kasumigaura station location, at the borehole (left) and surface (right) levels.

Fig. A.13. Validation of EXSIM generating synthetic ground motion acceleration time series: overlay of recorded accelerations and the corresponding generated signals for relatively close (150 km) and distant (300 km) distance from the hypocenter.

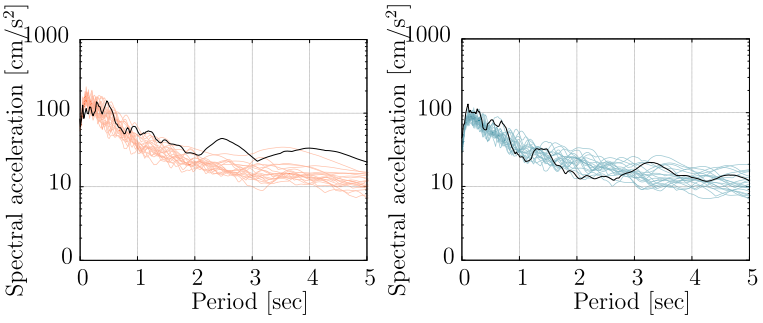

(a) Elastic response spectra calculated for Iwate prefecture, IWT023 - Kamaishi (left) and Ibaraki prefecture, IBRH17 - Kasumigaura station locations (right).

Fig. A.14. Validation of EXSIM generating synthetic ground motion acceleration time series: elastic response spectra considering 5% damping. Black lines represent the spectra generated from the recorded signal and color lines represent the spectra obtained from synthetic accelerograms. (For interpretation of the references to color in this figure legend, the reader is referred to the web version of this article.)

acceleration presented in Fig. A.13. The correlation of spectra at the more distant IBRH17 station presents a better agreement of the spectra than the correlations at the closer IWA23 station, as in the time-histories correlations. Again, the definitions of source parameters and the attenuation law selected to model seismic waves propagation of such extreme and rare event are most likely the

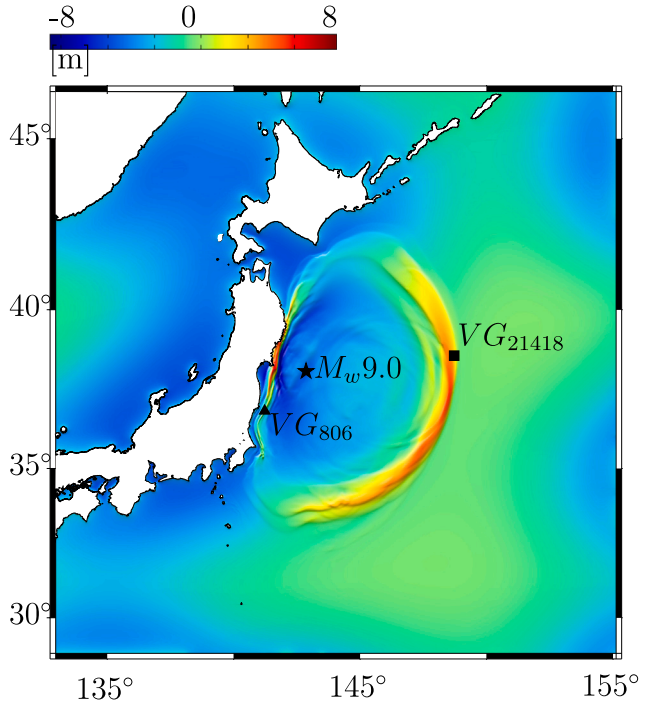

Fig. A.15. Validation of Eulerian NLSW-FV scheme: Tohoku-Oki, 2011 tsunami propagation at $t = 1800\,\mathrm{s}$. Location of the virtual gauges, VG, adopted to perform a numerical convergence analysis, which correspond to deep-ocean DART21418 and coastal GPS806 buoys.

reasons for the observed differences. GMM follow probabilistic analyses, making calibration of models to represent extreme events challenging and associated with uncertainty.

In conclusion, the tools adopted to characterize seismic acceleration in terms of peak, time.histories and response spectra demonstrate t be efficient to provide solutions for a range of accelerations and source-to-site distances that are similar to the extreme 1755-alike event characterized in Section 3.

A.2. Tsunami models

The performance of the NLSW-FV tool has been validated through an exhaustive benchmarking process, composed of verification (mass conservation, stability and convergence) and validation tests using data from different provenience, including analytical, experimental, and field data [22,23,81]. For the sake of conciseness, the numerical solutions of 2D train of waves are correlated with instrumentally recorded data from the 2011 Tohoku-Oki event at two representative locations. One corresponds to the location of a DART buoy, 500 km away from the epicenter, 650 km from the coast and 6 km-deep ocean (DART21418), while the other is a coastal GPS buoy (GPS806 - Fukushima), about 20 km from the shoreline, implemented in a ≈100 m-shallow area (see Fig. A.15).

The initial condition of the simulation adopts the source rupture parameters proposed by Fujii et al. 2011 [72], which has vertical co-seismic deformation with heterogeneous slip distribution, implemented in the Mirone software [34]. The solutions of tsunami propagation induced by the seafloor vertical displacements are computed using the NLSW-FV tool over physical time of the numerical simulation $t_f = 9200\,\mathrm{s}$ to include the first tsunami measurements acquired by the different buoys. A transmission boundary was prescribed on the outward limit of the computational domain. A convergence analysis using uniformly spaced grids of $\Delta x = \Delta y = 1500\,\mathrm{m}$, $\Delta x = \Delta y = 700\,\mathrm{m}$ and $\Delta x = \Delta y = 450\,\mathrm{m}$ obtained from the General Bathymetric Chart of the Oceans (GEBCO) dataset (see Data Availability Statement).

Fig. A.16 shows the comparison between instrumentally-recorded data and numerical solutions using $\Delta x = \Delta y = 700\,\mathrm{m}$ at virtual gauges implemented at locations corresponding to the buoys. For the deep-ocean DART21418 buoy, both the waveform and peak values of $\eta_{max} \approx 2\,\mathrm{m}$ are in good agreement with the recorded data. Similarly, for the close-to-shoreline GPS806 buoy data, the peak value of η and arrival of approximately thirty minutes (≈1800 s) after tsunami generation are in good agreement with recorded data. However, past approximately one hour (≈3600 s) the waveform is slightly less coincidental than the correlation for deep-sea location. Reasons for the differences can be varied, such as local topo-bathymetric influence imposed by ocean floor and coastal morphology, which can induce a series of reflection and refraction phenomena that are not as well captured. Thus, the misfit between the simulated and recorded waveform becomes more evident after approximately 4500 s of simulation time. Additional virtual gauges could be implemented, as indicated in Reis et al. [23].

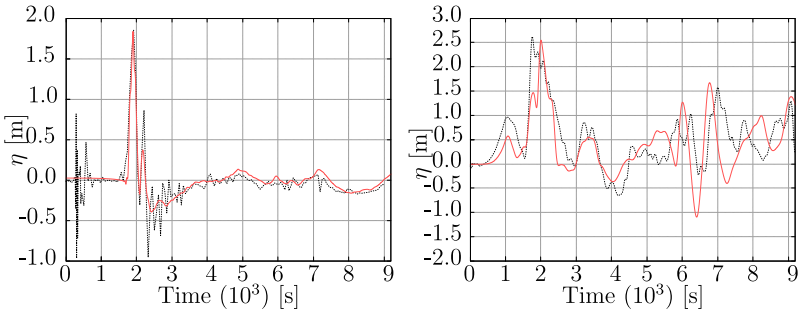

Fig. A.16. Validation of Eulerian NLSW-FV scheme: recorded data and numerical solution at buoy DART21418 (left) and the GPS806 buoy (right).

A.3. NS-SPH numerical scheme

The NS-SPH scheme has been gaining popularity among various fields of investigation, such as coastal engineering [25,82–84]. Over the last decade, the DualSPHysics code [24,25] has been adapted to tackle a wider range of physical phenomena. To model tsunami-like waves and tsunami interaction with coastal infrastructures, complementary algorithms have been added to the original numerical scheme. As part of the benchmarking of NS-SPH, some algorithms applicable to coastal engineering problems were studied, such as moving and open boundary conditions, solid–fluid and liquid–fluid interactions, and coupling techniques to reduce the domain estimated via DualSPHysics to strictly necessary regions with highly nonlinear phenomena.

Altomare et al. 2015 [82] coupled the SWASH code, which is a time-domain wave model based on a finite difference method for simulating sea waves generation and propagation in large domains, with DualSPHysics to model the area close to the coastline and provide a detailed description of the interaction between sea waves and coastal structures. Later, Altomare et al. 2020 [65] used SPH to perform a 3D model of a storm wave impacting a pier. Using an inlet boundary condition to generate the wave close to the structure and scaling the prototype to 1:10 allowed for a reduction in computational costs and an investigation of the pier's severe damage. Reis et al. [20,21] modeled the impact of tsunami-like waves on an elevated structure using a coupled technique on which a NLSW-FV code is adopted to model tsunami waves' generation and propagation, while the NS-SPH scheme implemented in DualSPHysics is responsible for the characterization of tsunami forces and pressures on the elevated structure, both in horizontal and vertical directions. The latter coupled model represents about 50% of computational savings on a laboratory campaign scale. The authors extrapolated the conclusions for real coastal engineering problems, where the scale of the tsunami propagation phase is much more extensive than the inundation and fluid-interaction phases of the experimental campaign, predicting a greater expression of the advantages of coupling algorithms, since the Eulerian scheme would be employed in a very large fraction of the computation domain. In order to keep this article concise, and in light of the extensive validation that NS-SPH and coupled techniques have already experienced [20,21], qualitative modeling aspects of the 2011 Japan Tsunami interacting with a critical infrastructure on the Japanese coast are here discussed to highlight considerations for modeling a historic events where no data is available, such as the case-study analyzed in this paper.

References

[1] EC, Migration and Home Affairs of European Commission, Critical infrastructure, 2013, URL https://home-affairs.ec.europa.eu/pages/page/critical-infrastructure_en.

[2] United Nations Office for Disaster Risk Reduction, UNDRR, Critical Infrastructure (in the framework of Sendai framework terminology), 2015, URL https://www.undrr.org/terminology/critical-infrastructure.

[3] Department of Homeland Security, US, Critical infrastructure, 2023, URL https://www.dhs.gov/science-and-technology/critical-infrastructure.

[4] CISA, Cibersecurity and Infrastructure Security Agency, Critical infrastructure sectors, 2023, URL https://www.cisa.gov/topics/critical-infrastructure-security-and-resilience/critical-infrastructure-sectors.

[5] C. Reis, M.A. Baptista, M. Lopes, C.S. Oliveira, S. Clain, C. Sousa Oliveira, S. Clain, C.S. Oliveira, S. Clain, C. Sousa Oliveira, S. Clain, Cascade earthquake and tsunami hazard assessment : A deterministic perspective for engineering purposes, Int. J. Disaster Risk Reduct. submitted (102952) (2022) http://dx.doi.org/10.1016/j.ijdrr.2022.102952.

[6] H.M. Fritz, C.M. Petroff, P.A. Catalán, R. Cienfuegos, P. Winckler, N. Kalligeris, R. Weiss, S.E. Barrientos, G. Meneses, C. Valderas-Bermejo, C. Ebeling, A. Papadopoulos, M. Contreras, R. Almar, J.C. Dominguez, C.E. Synolakis, Field survey of the 27 february 2010 Chile tsunami, Pure Appl. Geophys. 168 (11) (2011) 1989–2010, http://dx.doi.org/10.1007/s00024-011-0283-5.

[7] A. Pomonis, K. Saito, S. Fraser, S.C. Chian, K. Goda, J. Macabuag, M. Offord, A. Raby, P. Sammonds, E. Gavanski, M. Koyama, H. Murakami, T. Rossetto, D. Grant, J.E. Alarcon, EEFIT Field Report: The Mw9.0 Tōhoku Earthquake and Tsunami of 11th March, Tech. Rep. March, Earthquake Engineering Field Investigation Team, United Kigdom, 2011, p. 204.

[8] T. Sugano, A. Nozu, E. Kohama, K.I. Shimosako, Y. Kikuchi, Damage to coastal structures, Soil Found. 54 (4) (2014) 883–901, http://dx.doi.org/10.1016/j.sandf.2014.06.018.

[9] I. Charvet, J. Macabuag, T. Rossetto, Estimating tsunami-induced building damage through fragility functions: Critical review and research needs, Front. Built Environ. 3 (August) (2017) 1–22, http://dx.doi.org/10.3389/fbuil.2017.00036.

[10] Y. Cheng, E.A. Elsayed, X. Chen, Random multi hazard resilience modeling of engineered systems and critical infrastructure, Reliab. Eng. Syst. Saf. 209 (December 2020) (2021) 107453, http://dx.doi.org/10.1016/j.ress.2021.107453.

[11] S.A. Argyroudis, S.A. Mitoulis, L. Hofer, M.A. Zanini, E. Tubaldi, D.M. Frangopol, Resilience assessment framework for critical infrastructure in a multi-hazard environment: Case study on transport assets, Sci. Total Environ. 714 (2020) 1–49, http://dx.doi.org/10.1016/j.scitotenv.2020.136854.
[12] J. Verschuur, E.E. Koks, J.W. Hall, Ports' criticality in international trade and global supply-chains, Nature Commun. 13 (1) (2022) 1–13, http://dx.doi.org/10.1038/s41467-022-32070-0.
[13] J. Verschuur, E.E. Koks, J.W. Hall, Port disruptions due to natural disasters: Insights into port and logistics resilience, Transp. Res. D 85 (May) (2020) 102393, http://dx.doi.org/10.1016/j.trd.2020.102393.
[14] J. Verschuur, E.E. Koks, S. Li, J.W. Hall, Multi-hazard risk to global port infrastructure and resulting trade and logistics losses, Commun. Earth Environ. 4 (1) (2023) 1–12, http://dx.doi.org/10.1038/s43247-022-00656-7.
[15] A. Suppasri, E. Maly, M. Kitamura, G. Pescaroli, D. Alexander, F. Imamura, Cascading disasters triggered by tsunami hazards: A perspective for critical infrastructure resilience and disaster risk reduction, Int. J. Disaster Risk Reduct. 66 (102597) (2021) http://dx.doi.org/10.1016/j.ijdrr.2021.102597.
[16] J.S.L. Lam, J.A. Lassa, Risk assessment framework for exposure of cargo and ports to natural hazards and climate extremes, Marit. Policy Manag. 44 (1) (2017) 1–15, http://dx.doi.org/10.1080/03088839.2016.1245877.
[17] C.T. Chua, A.D. Switzer, A. Suppasri, L. Li, K. Pakoksung, D. Lallemant, S.F. Jenkins, I. Charvet, T. Chua, A. Cheong, Tsunami damage to ports : Cataloguing damage to create fragility functions from the 2011 Tohoku event, Nat. Hazard Earth Sci. in review (October) (2020) 1–37, http://dx.doi.org/10.5194/nhess-2020-355.
[18] R. De Risi, K. Goda, T. Yasuda, N. Mori, Is flow velocity important in tsunami empirical fragility modeling? Earth-Sci. Rev. 166 (2017) 64–82, http://dx.doi.org/10.1016/j.earscirev.2016.12.015.
[19] G.M. Atkinson, K. Assatourians, Implementation and validation of EXSIM (a stochastic finite-fault ground-motion simulation algorithm) on the SCEC broadband platform, Seismol. Res. Lett. 86 (1) (2015) 48–60, http://dx.doi.org/10.1785/0220140097.
[20] C. Reis, S.S.S. Clain, J. Figueiredo, M.A. Baptista, M.M. Lopes, A.R. Barbosa, M.A. Baptista, M.M. Lopes, A.R. Barbosa, M.A. Baptista, M.M. Lopes, Experimentally validated numerical models to assess tsunami hydrodynamic force on an elevated structure, Eng. Struct. Accepted (September) (2021) http://dx.doi.org/10.1016/j.engstruct.2021.113280.
[21] C. Reis, A.R. Barbosa, J. Figueiredo, S. Clain, M. Lopes, M.A. Baptista, Smoothed Particle Hydrodynamics modeling of elevated structures impacted by tsunami-like waves, Eng. Struct. 270 (114851) (2022) http://dx.doi.org/10.1016/j.engstruct.2022.114851.
[22] S. Clain, C. Reis, R. Costa, J. Figueiredo, M.A. Baptista, J.M. Miranda, Second-order finite volume with hydrostatic reconstruction for tsunami simulation, J. Adv. Modelling Earth Syst. 8 (4) (2016) 1691–1713, http://dx.doi.org/10.1002/2015MS000603.
[23] C. Reis, J. Figueiredo, S. Clain, R. Omira, M.A. Baptista, J.M. Miranda, Comparison between MUSCL and MOOD techniques in a finite volume well-balanced code to solve SWE. The Tohoku-Oki, 2011 example, Geophys. J. Int. (2018) http://dx.doi.org/10.1093/gji/ggy472.
[24] A.J.C. Crespo, J.M. Domínguez, B.D. Rogers, M. Gómez-Gesteira, S. Longshaw, R.J.F.B. Canelas, R. Vacondio, A. Barreiro, O. García-Feal, DualSPHysics: Open-source parallel CFD solver based on Smoothed Particle Hydrodynamics (SPH), Comput. Phys. Comm. 187 (2015) 204–216, http://dx.doi.org/10.1016/j.cpc.2014.10.004.
[25] J.M. Domínguez, G. Fourtakas, C. Altomare, R.J.F.B. Canelas, A. Tafuni, O. García-Feal, I. Martínez-Estévez, A. Mokos, R. Vacondio, A.J.C. Crespo, B.D. Rogers, P.K. Stansby, M. Gómez-Gesteira, DualSPHysics: from fluid dynamics to multiphysics problems, Comput. Part. Mech. (2021) http://dx.doi.org/10.1007/s40571-021-00404-2.
[26] C. Reis, M. Lopes, M.A. Baptista, S. Clain, Towards an integrated framework for the risk assessment of coastal structures exposed to earthquake and tsunami hazards, Resil. Cities Struct. Submitted (2022).
[27] D. Motazedian, G.M. Atkinson, Stochastic finite-fault modeling based on a dynamic corner frequency, Bull. Seismol. Soc. Am. 95 (3) (2005) 995–1010, http://dx.doi.org/10.1785/0120030207.
[28] D.M. Boore, Stochastic simulation of high-frequency ground motions based on seismological models of the radiated spectra, Bull. Seismol. Soc. Am. 73 (1983) 1865–1894.
[29] D.M. Boore, Simulation of ground motion using the stochastic method, Pure Appl. Geophys. 160 (3–4) (2003) 635–676, http://dx.doi.org/10.1007/PL00012553.
[30] J.N. Brune, Tectonic stress and the spectra of seismic shear waves from earthquakes, J. Geophys. Res. 75 (26) (1970) 4997–5009, http://dx.doi.org/10.1029/JB075i026p04997, URL http://doi.wiley.com/10.1029/JB075i026p04997.
[31] O.C. Blender, Blender - A 3D modelling and rendering package, 2018.
[32] K. Kajiura, Tsunami source, energy and directivity of wave radiation, Bull. Earthq. Res. Inst. 48 (1970) 835–869.
[33] Y. Okada, Surface deformation due to shear and tensile faults in a Half-Space, Bull. Seismol. Soc. Am. 75 (4) (1985) 1135–1154.
[34] J.F. Luis, Mirone: A multi-purpose tool for exploring grid data, Comput. Geosci. 33 (1) (2007) 31–41, http://dx.doi.org/10.1016/j.cageo.2006.05.005.
[35] M. Wronna, R. Omira, M.A. Baptista, Deterministic approach for multiple-source tsunami hazard assessment for Sines, Portugal, Nat. Hazards Earth Syst. Sci. 15 (11) (2015) 2557–2568, http://dx.doi.org/10.5194/nhess-15-2557-2015.
[36] A. Tafuni, J.M. Domínguez, R. Vacondio, A.J.C. Crespo, A versatile algorithm for the treatment of open boundary conditions in smoothed particle hydrodynamics GPU models, Comput. Methods Appl. Mech. Engrg. 342 (2018) 604–624, http://dx.doi.org/10.1016/j.cma.2018.08.004.
[37] M.R. Motley, M.O. Eberhard, P. Arduino, A.R. Barbosa, Probabilistic Assessment of Tsunami Forces on Coastal Structures, Tech. rep., DesignSafe, 2019, http://dx.doi.org/10.17603/ds2-q2w5-0t48.
[38] A.O. Winter, M.S. Alam, K. Shekhar, M.R. Motley, M.O. Eberhard, A.R. Barbosa, P. Lomonaco, P. Arduino, D.T. Cox, Tsunami-like wave forces on an elevated coastal structure: Effects of flow shielding and channeling, J. Waterw. Port Coast. Ocean Eng. 146 (4) (2020) 1–24, http://dx.doi.org/10.1061/(ASCE)WW.1943-5460.0000562.
[39] M.S. Alam, A.O. Winter, G. Galant, K. Shekhar, A.R. Barbosa, M.R. Motley, M.O. Eberhard, D.T. Cox, P. Arduino, P. Lomonaco, Tsunami-like wave-induced lateral and uplift pressures and forces on an elevated coastal structure, J. Waterw. Port Coast. Ocean Eng. 146 (4) (2020) 1–18, http://dx.doi.org/10.1061/(ASCE)WW.1943-5460.0000562.
[40] J.J. Monaghan, Smoothed particle hydrodynamics, Annu. Rev. Astron. Astrophys. 30 (1) (1992) 543–574.
[41] S.P.A. APS, Port of Sines. URL https://www.apsinesalgarve.pt/en/ports/port-of-sines/.
[42] P.G.P. Portal Diplomatic, The secretary of state visits the Sines port logistical and industrial complex.pdf, Communication and media.
[43] P.G. Silva, J. Elez, R. Pérez-López, J.L. Giner-Robles, P.V. Gómez-Diego, E. Roquero, M.Á. Rodríguez-Pascua, T. Bardají, The AD 1755 Lisbon earthquake-tsunami: Seismic source modelling from the analysis of ESI-07 environmental data, Quat. Int. (2021) http://dx.doi.org/10.1016/j.quaint.2021.11.006.
[44] M.A. Baptista, J.M. Miranda, F. Chierici, N. Zitellini, New study of the 1755 earthquake source based on multi-channel seismic survey data and tsunami modeling, Nat. Hazards Earth Syst. Sci. 3 (5) (2003) 333–340.
[45] A.C. Johnston, Seismic moment assessment of earthquakes in stable continental regions - III. New Madrid 1811-1812, Charleston 1886 and Lisbon 1755, Geophys. J. Int. 126 (1996) 314–344.
[46] R. Grandin, J.F. Borges, M. Bezzeghoud, B. Caldeira, F. Carrilho, Simulations of strong ground motion in SW Iberia for the 1969 February 28 (Ms8.0) and the 1755 November 1 (M8.5) earthquakes - II. Strong ground motion simulations, Geophys. J. Int. 171 (2) (2007) 807–822, http://dx.doi.org/10.1111/j.1365-246X.2007.03571.x.

[47] M.A. Gutcher, J. Malod, J.P. Rehault, I. Contrucci, F. Klingelhoefer, L.A. Mendes-Victor, W. Spakman, Evidence for active subduction beneath Gibraltar, Geology 31 (1) (2003) 1071–1074, http://dx.doi.org/10.1130/0091-7613-31.1.e22.
[48] N. Zitellini, L.A. Mendes, D. Cordoba, J. Danobeitia, R. Nicolich, G. Pellis, A. Ribeiro, R. Sartori, L. Torelli, R. Bartolomé, G. Bortoluzzi, A. Calafato, F. Carrilho, L. Casoni, E. Chierici, C. Corela, A. Correggiari, B. Delia Vedova, E. Gracia, P. Jornet, M. Landuzzi, M. Ligi, A. Magagnoli, G. Marozzi, L. Matias, D. Penitenti, P. Rodriguez, M. Rovere, P. Terrinha, L. Vigliotti, A.Z. Ruiz, Source of 1755 lisbon earthquake and tsunami investigated, Eos 82 (26) (2001) 285–291, http://dx.doi.org/10.1029/EO082i026p00285-01.
[49] P. Terrinha, L.M. Pinheiro, J.P. Henriet, L. Matias, M. Ivanov, J.H. Monteiro, A. Akhmetzhanov, A. Volkonskaya, T.A. Cunha, P. Shaskin, M. Rovere, Tsunamigenic-seismogenic structures, neotectonics, sedimentary processes and slope instability on the southwest Portuguese Margin, Mar. Geol. 195 (1–4) (2003) 55–73, http://dx.doi.org/10.1016/S0025-3227(02)00682-5.
[50] L. Matias, T.A. Cunha, A. Annunziato, M.A. Baptista, F. Carrilho, Tsunamigenic earthquakes in the Gulf of Cadiz: fault model and recurrence, Nat. Hazards Earth Syst. Sci. 13 (1) (2013) 1–13, http://dx.doi.org/10.5194/nhess-13-1-2013.
[51] F.M. Rosas, J.C. Duarte, W.P. Schellart, R. Tomás, P. Terrinha, Seismic potential of thrust-wrench tectonic interference between major active faults offshore SW Iberia: A new explanation for the 1755 Great Lisbon Earthquake? in: J.C. Duarte, W.P. Schellart (Eds.), Plate Boundaries and Natural Hazards, Geophysical Monograph, first ed., American Geophysical Union, 2016, pp. 193–217, http://dx.doi.org/10.1002/9781119054146.ch9, Ch. Chapter 9.
[52] J.C. Duarte, F.M. Rosas, P. Terrinha, W.P. Schellart, D. Boutelier, M.A. Gutscher, A. Ribeiro, Are subduction zones invading the Atlantic? Evidence from the southwest Iberia margin, Geology 41 (8) (2013) 839–842, http://dx.doi.org/10.1130/G34100.1.
[53] G.M. Atkinson, D.M. Boore, Ground-motion relations for eastern north America, Bull. Seismol. Soc. Am. 85 (5) (1995) 1327–1342, http://dx.doi.org/10.1785/0120050245.
[54] A. Ribeiro, L.A. Mendes-Victor, J.M.L.C. Cabral, L.M. Matias, P.A.G. Terrinha, The 1755 Lisbon earthquake and the beginning of closure of the Atlantic, Eur. Rev. 14 (2) (2006) 193–205, http://dx.doi.org/10.1017/S1062798706000196.
[55] A. Ribeiro, J. Cabral, L. Matias, Stress pattern in Portugal mainland and the adjacent Atlantic region West Iberia, Tectonics 15 (2) (1996) 641–659, http://dx.doi.org/10.1029/95tc03683.
[56] G. Zonno, A. Carvalho, G. Franceschina, A. Akinci, A. Campos-Costa, E. Coelho, G. Cultrera, F. Pacor, V. Pessina, M. Cocco, Simulating earthquake scenarios using finite-fault model for the Metropolitan Area of Lisbon (MAL), in: L.A. Mendes-Victor, C.S. Oliveira, J. Azevedo, A. Ribeiro (Eds.), 250th Anniversary of the 1755 Lisbon Earthquake, Springer Science & Business Media, Milan, Italy, 2005.
[57] A. Carvalho, A.C. Costa, C. Sousa Oliveira, C.S. Oliveira, C. Sousa Oliveira, C.S. Oliveira, A finite-fault modeling of the 1755 Lisbon earthquake sources, in: Geotechnical, Geological and Earthquake Engineering, Vol. 7, 2009, pp. 433–454, http://dx.doi.org/10.1007/978-1-4020-8609-0_28.
[58] A. Carvalho, C. Reis, D. Vales, Source and high-frequency decay parameters for the Azores region for stochastic finite-fault ground motion simulations, Bull. Earthq. Eng. 14 (7) (2016) 1885–1902, http://dx.doi.org/10.1007/s10518-015-9842-y.
[59] D.L. Wells, K.J. Coppersmith, New Empirical Relationships Among Magnitude, Rupture Length, Rupture Width, Rupture Area, and Surface Displacement, Vol. 84, 1994, pp. 974–1002.
[60] G.M. Atkinson, D.M. Boore, Earthquake ground-motion prediction equations for eastern North America, Bull. Seismol. Soc. Am. (2006) http://dx.doi.org/10.1785/0120050245.
[61] E. Buckingham, On physically similar systems; Illustrations of the use of dimensional equations, Phys. Rev. 4 (4) (1914) 345–376, http://dx.doi.org/10.1103/PhysRev.4.345.
[62] A.J. Rosakis, J.E. Andrade, V. Gabuchian, J.M. Harmon, J.P. Conte, J.I. Restrepo, A. Rodriguez, A. Nema, A.R. Pedretti, Implications of Buckingham's Pi theorem to the study of similitude in discrete structures: Introduction of the RFN, μN, and SN dimensionless numbers and the concept of structural speed, J. Appl. Mech. Trans. ASME 88 (9) (2021) http://dx.doi.org/10.1115/1.4051338.
[63] E. Didier, M.G. Neves, A semi-infinite numerical wave flume using smoothed particle hydrodynamics, Int. J. Offshore Polar Eng. 22 (3) (2012) 193–199.
[64] E. Didier, D.R.C.B. Neves, R. Martins, M.G. Neves, Wave interaction with a vertical wall: SPH numerical and experimental modeling, Ocean Eng. 88 (2014) 330–341, http://dx.doi.org/10.1016/j.oceaneng.2014.06.029.
[65] C. Altomare, A. Tafuni, J.M. Domínguez, A.J.C. Crespo, X. Gironella, J. Sospedra, SPH simulations of real sea waves impacting a large-scale structure, J. Mar. Sci. Eng. 8 (10) (2020) 1–21, http://dx.doi.org/10.3390/jmse8100826.
[66] I.M.I. Qeshta, M.J. Hashemi, M.R. Hashemi, R.J. Gravina, S. Setunge, Development of fragility functions for rigid-frame bridges subjected to tsunami-induced hydrodynamic forces, Struct. Infrastruct. Eng. (2021) 1–18, http://dx.doi.org/10.1080/15732479.2021.1892774.
[67] C. Petrone, T. Rossetto, K. Goda, I. Eames, Tsunami analysis of structures: Comparison among different approaches, in: 16th World Conference on Earthquake, 16WCEE, Santiago, Chile, 2017, Paper No. 3706.
[68] T. Tomiczek, A. Wyman, H. Park, D.T. Cox, Modified Goda equations to predict pressure distribution and horizontal forces for design of elevated coastal structures, J. Waterw. Port Coast. Ocean Eng. 145 (6) (2019) 1–16, http://dx.doi.org/10.1061/(asce)ww.1943-5460.0000527.
[69] M. Pagani, D. Monelli, G. Weatherill, L. Danciu, H. Crowley, V. Silva, P. Henshaw, L. Butler, M. Nastasi, L. Panzeri, M. Simionato, D. Vigano, Openquake engine: An open hazard (and risk) software for the global earthquake model, Seismol. Res. Lett. 85 (3) (2014) 692–702, http://dx.doi.org/10.1785/0220130087.
[70] Y. Tang, Y. Yin, K. Hill, V. Katiyar, A. Nasseri, T. Lai, Seismic risk assessment of lisbon metropolitan area under a recurrence of the 1755 earthquake with tsunami inundation, in: 15th World Conference on Earthquake Engineering (15WCEE), Lisbon, Portugal, 2012.
[71] S. Ozawa, T. Nishimura, H. Suito, T. Kobayashi, M. Tobita, T. Imakiire, Coseismic and postseismic slip of the 2011 magnitude-9 Tohoku-Oki earthquake, Nature 475 (7356) (2011) 373–377, http://dx.doi.org/10.1038/nature10227.
[72] Y. Fujii, K. Satake, S. Sakai, M. Shinohara, T. Kanazawa, Tsunami source of the 2011 off the Pacific Coast of Tohoku earthquake, Earth Planets Space 63 (7) (2011) 815–820.
[73] Y. Yokota, K. Koketsu, Y. Fujii, K. Satake, S. Sakai, M. Shinohara, T. Kanazawa, Joint inversion of strong motion, teleseismic, geodetic, and tsunami datasets for the rupture process of the 2011 Tohoku earthquake, Geophys. Res. Lett. 38 (24) (2011) 1–5, http://dx.doi.org/10.1029/2011GL050098.
[74] N. Maercklin, G. Festa, S. Colombelli, A. Zollo, Twin ruptures grew to build up the giant 2011 Tohoku, Japan, earthquake, Sci. Rep. 2 (2012) http://dx.doi.org/10.1038/srep00709.
[75] G.M. Atkinson, D.M. Boore, Empirical ground-motion relations for subduction-zone earthquakes and their application to Cascadia and other regions, Bull. Seismol. Soc. Am. 93 (4) (2003) 1703–1729, http://dx.doi.org/10.1785/0120020156.
[76] N.A. Abrahamson, W.J. Silva, R. Kamai, Summary of the ASK14 ground motion relation for active crustal regions, Earthq. Spectra 30 (3) (2014) 1025–1055, http://dx.doi.org/10.1193/070913EQS198M.
[77] D.M. Boore, J.P. Stewart, E. Seyhan, G.M. Atkinson, NGA-West2 equations for predicting PGA, PGV, and 5% damped PSA for shallow crustal earthquakes, Earthq. Spectra 30 (3) (2014) 1057–1085, http://dx.doi.org/10.1193/070113EQS184M.
[78] K.W. Campbell, Y. Bozorgnia, NGA-West2 ground motion model for the average horizontal components of PGA, PGV, and 5% damped linear acceleration response spectra, Earthq. Spectra 30 (3) (2014) 1087–1114, http://dx.doi.org/10.1193/062913EQS175M.
[79] H. Si, S. Midorikawa, T. Kishida, Development of NGA-sub ground-motion model of 5% damped pseudo-spectral acceleration based on database for subduction earthquakes in Japan, Earthq. Spectra I (25) (2022) http://dx.doi.org/10.1177/87552930221090326.
[80] H. Ghofrani, G.M. Atkinson, K. Goda, K. Assatourians, Stochastic finite-fault simulations of the 2011 Tohoku, Japan, earthquake, Bull. Seismol. Soc. Am. 103 (2 B) (2013) 1307–1320, http://dx.doi.org/10.1785/0120120228.

[81] C. Reis, J. Figueiredo, S. Clain, R. Omira, M.A. Baptista, J.M. Miranda, MUSCL vs MOOD techniques to solve the SWE in the framework of tsunami events, in: SYMCOMP 2017 - 3rd International Conference on Numerical and Symbolic Computation: Developments and Applications, Proceedings, Guimarães, Portugal, 2017, pp. 189–204.

[82] C. Altomare, J.M. Domínguez, A.J.C. Crespo, T. Suzuki, I. Caceres, M. Gómez-Gesteira, Hybridization of the wave propagation model SWASH and the meshfree particle method SPH for real coastal applications, Coast. Eng. J. 57 (04) (2015) 1550024, http://dx.doi.org/10.1142/S0578563415500242.

[83] H. Gotoh, A. Khayyer, On the state-of-the-art of particle methods for coastal and ocean engineering, Coast. Eng. J. 60 (1) (2018) 79–103, http://dx.doi.org/10.1080/21664250.2018.1436243.

[84] S.J. Lind, B.D. Rogers, P.K. Stansby, Review of smoothed particle hydrodynamics: towards converged Lagrangian flow modelling, Proc. R. Soc. A 476 (2241) (2020) 20190801, http://dx.doi.org/10.1098/rspa.2019.0801.